Soft Matter

REVIEW

View Article Online
View Journal | View Issue

Cite this: *Soft Matter*, 2022, **18**, 4042

Solvent-assisted self-assembly of block copolymer thin films

Przemyslaw Pula, Arkadiusz Leniart and Pawel W. Majewski *

Solvent-assisted block copolymer self-assembly is a compelling method for processing and advancing practical applications of these materials due to the exceptional level of the control of BCP morphology and significant acceleration of ordering kinetics. Despite substantial experimental and theoretical efforts devoted to understanding of solvent-assisted BCP film ordering, the development of a universal BCP patterning protocol remains elusive; possibly due to a multitude of factors which dictate the self-assembly scenario. The aim of this review is to aggregate both seminal reports and the latest progress in solvent-assisted directed self-assembly and to provide the reader with theoretical background, including the outline of BCP ordering thermodynamics and kinetics phenomena. We also indicate significant BCP research areas and emerging high-tech applications where solvent-assisted processing might play a dominant role.

Received 5th April 2022,
Accepted 16th May 2022

DOI: 10.1039/d2sm00439a

rsc.li/soft-matter-journal

Scope of the review and introduction

Block copolymers (BCP) constitute an important class of self-assembling materials consisting of two or more chemically dissimilar polymeric chains called blocks. Progress in BCP science has been documented by numerous reviews focused on their synthesis,[1–3] processing,[4–10] and their applications.[6,11–16] Arguably, the greatest advantage of BCP-mediated manufacturing of nanoscale patterns is the low-cost and high-throughput of this approach compared to the conventional methods such as photo- and e-beam lithography. Numerous applications for BCP-ordered templates have been proposed, including optical coatings,[17,18] metamaterials,[19–21] photonic crystals,[22,23] plasmonic nanostructures,[24,25] and membranes.[26,27] These emerging applications have propelled research efforts aimed at understanding and harnessing the self-assembly of BCP thin films and led to the development of various directed self-assembly (DSA†) methods. DSA methods are used to accelerate the self-assembly process and to reduce patterns' defectivity to an application enabling level and, by using directional biases, to orient (align) anisotropic BCP morphologies.[4,8,10,28]

Department of Chemistry, University of Warsaw, Warsaw 02089, Poland.
E-mail: pmajewski@chem.uw.edu.pl

† Here, we use the DSA term to encompass any method that directs the BCP self-assembly.[7,8] More narrowly, it has been used in the context of graphoepitaxial and chemoepitaxial ordering.[28–30]

Przemyslaw Pula

Przemysław Puła obtained his MSc degree in Nanostructure Engineering in 2019 from the Department of Physics at the University of Warsaw. In the same year, he started his PhD studies under the supervision of Prof. Majewski. His research is focused on self-assembly of block copolymer-low molecular weight compounds blends and their use in fabrication of volatile organic compound gas sensors.

Arkadiusz Leniart

Arkadiusz Leniart is currently a PhD candidate in Chemistry at the University of Warsaw. He received his M.Sc. degree in Physics in 2017. His research focuses on directed self-assembly of block copolymer thin films and development of photothermal and solvent-assisted annealing methods enabling rapid fabrication of ordered nanostructured coatings. Besides his scientific activity, he is also a professional chess player awarded with the Grandmaster title.

Polymer–solvent interactions are at the core of polymer and block copolymer science since their discovery, therefore providing a complete review of this topic exceeds the capacity of this publication. Instead, we focus on solvent-driven or solvent-assisted self-assembly of block copolymers leading to the formation of nanoscale patterns in thin films (10–1000 nm). We have also limited our discussion of BCP self-assembly in solution, thoroughly reviewed elsewhere,[29,30] only to the aspects necessary to understand BCP–solvent interactions in concentrated solutions and solvent–swollen polymer films near and above the onset of the order–disorder phase transition concentration. A complete overview of BCP–solvent interactions over an entire concentration range including a thorough presentation of phase behavior can be found in the review by Alexandridis and Spontak.[31] Also, we omitted solvent-mediated assembly of BCP-nanoparticle hybrid films recently reviewed by other authors.[32–34] While this review focuses mainly on solvents liquid at room temperature, we would like to mention supercritical carbon dioxide ($scCO_2$) as an attractive alternative for polymer processing, including BCPs. We would like to point the readers to the excellent review of this topic by Walker *et al.*[35] and some more recent reports.[36–39]

The solution-processing compatibility of BCPs is perhaps one of their main advantages and is the reason for widespread interest in these nanomaterials. Understanding and controlling block copolymer–solvent interactions in thin films is of critical importance both for processing and practical patterning application. In this review, we focus on solvent-assisted BCP self-assembly and DSA techniques that utilize BCP–solvent interactions. Because solvent-assisted processing is probably one of the most facile DSA methods, it is frequently a method of choice for scientists who start research in these materials. At the same time, because of the intricate balance between the thermodynamics and kinetics that drives the self-assembly of BCP as well as the composition heterogeneity of the materials, it is notoriously difficult to control. These difficulties result in common pitfalls in the laboratory practice and, despite the best efforts, frequent inconsistencies in the reported results. For this reason, we first provide the reader with a theoretical overview of the topic. Then, we briefly describe popular BCP thin-film deposition techniques and present a toolbox of DSA methods, highlighting the critical practical aspects of experimental design and relate them to the major strategies of process control. As shown in Fig. 1, for the sake of clarity of presentation, we classified the reviewed DSA methods into two major categories: (i) direct casting methods in which BCP morphologies self-assemble concurrently with the material deposition step and (ii) post-casting annealing in which the BCP morphology is ordered after the casting step. We admit that in some cases, the division is rather arbitrary and we review such methods in a separate, hybrid methods category, along with more complex solvent-assisted DSA techniques, which utilize additional ordering biases such as shearing or surface-mediated interactions. Finally, we review the work dedicated to grain-coarsening kinetics and reduction of structural defects in BCP thin films.

We center our efforts on providing the reader with a practical guide to the topic and bring their attention to a limited number of selected research reports, frequently using them as an exemplary illustration of the discussed phenomena. Where possible, we provide a reference to more comprehensive, excellent review contributions by other authors.

Pawel W. Majewski

Pawel W. Majewski is an assistant professor in the Department of Chemistry at the University of Warsaw. He received his PhD in Chemical Engineering from Yale University in 2013 for studies of anisotropic charge transport in magnetically-ordered soft materials under the guidance of Prof. Chinedum Osuji. In the same year, he joined Prof. Oleg Gang's group at Brookhaven National Laboratory where he worked as a postdoctoral researcher under the supervision of Dr Kevin Yager investigating laser-induced self-assembly of BCP thin films using synchrotron X-ray scattering methods. Since 2016 he has been leading an experimental group that focuses on structure and functional properties of soft materials at the UW. His research interests include studies of photothermally directed self-assembly of block copolymers and liquid crystals, development of rapid methods for BCP patterning, and soft-material templated synthesis of functional nanostructured materials.

Overview of BCP–solvent interactions

Thermodynamic equilibrium between solvent vapor and solvent–swollen polymer

Polymer swelling induced by the sorption of solvent from a gas phase is analogous to the dissolution of the polymer in a liquid solvent. To promote solvent uptake, the thermodynamic driving force for polymer–solvent mixing, *i.e.*, the change in the Gibbs free energy, ΔG_{mix} must be negative:

$$\Delta G_{mix} = \Delta H_{mix} - T\Delta S_{mix} < 0, \quad (1)$$

where ΔH_{mix} and ΔS_{mix} are enthalpy and entropy of mixing, respectively.[46]

For nonpolar or weakly polar polymer–solvent systems, regular solution theory defines the thermodynamic equilibrium between the activity of solvent molecules (a) in the gas phase and in polymer solution:[47]

$$\frac{\mu_S - \mu_s^0}{k_B T} = \ln(a) = \ln\left(\frac{p}{p_{sat}}\right), \quad (2)$$

where p/p_{sat} is the degree of saturation of solvent vapor pressure and μ_S and μ_s^0 are chemical potentials of the pure solvent and solvent in the polymer solution. The degree of vapor

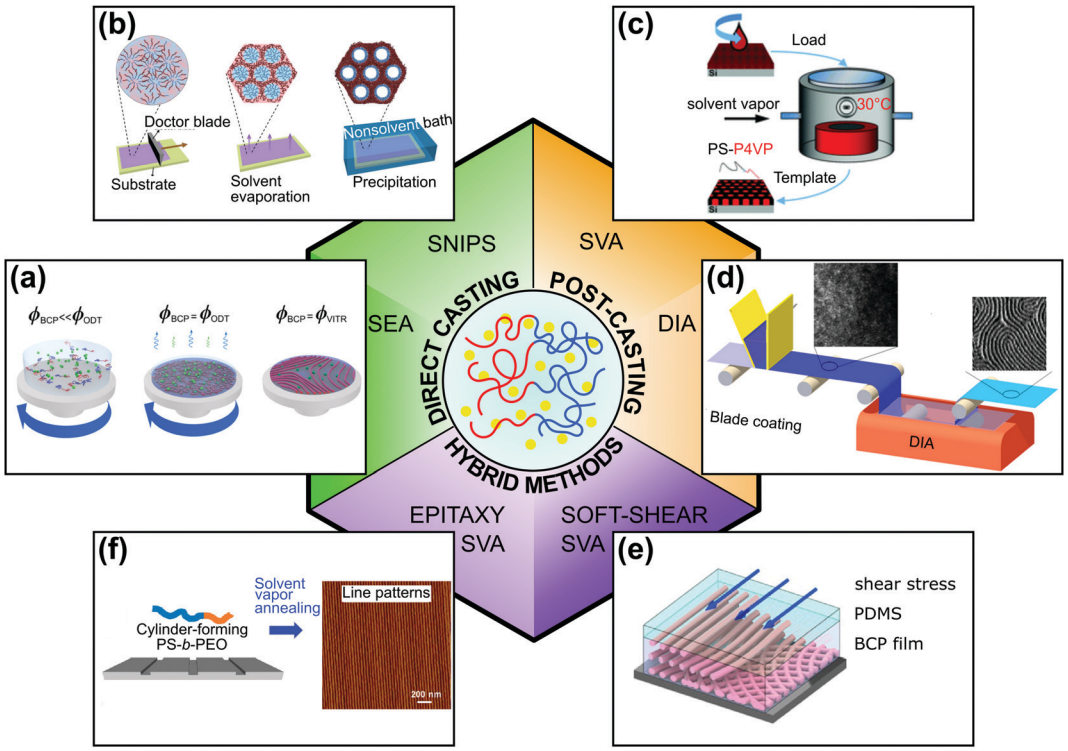

Fig. 1 Overview of solvent-assisted directed self-assembly of BCP films. (a) Solvent evaporation annealing, (b) self-assembly and non-solvent induced phase separation, (c) solvent vapor annealing, (d) direct immersion annealing. (e) Soft-shear solvent vapor annealing, (f) epitaxy combined with solvent vapor annealing. (a) Adapted with permission from *Macromolecules*, **54**, 11178.[40] Copyright 2020 American Chemical Society, (b) adapted from *Macromol. Rapid Commun.*, **42**, 2100235.[41] Copyright 2021 *Macromolecular Rapid Communications* published by Wiley-VCH GmbH, (c) adapted from *Phys. Chem. Chem. Phys.*, **19**, 2805.[42] with permission from the Royal Society of Chemistry, (d) adapted with permission from *ACS Appl. Mater. Interfaces*, **7**, 21639.[43] Copyright 2015 American Chemical Society, (e) adapted with permission from *Macromolecules*, **51**, 4213.[44] Copyright 2018 American Chemical Society (f) adapted with permission from *ACS Nano*, **10**, 7915.[45] Copyright 2016 American Chemical Society.

pressure saturation is related to the composition of the liquid phase by the Flory–Huggins law:[48]

$$\frac{\mu_S - \mu_s^0}{k_B T} = \chi_{PS}\phi_P{}^2 + \left(1 - \frac{v_S}{v_P}\right)\phi_P + \ln(1 - \phi_P), \quad (3)$$

where ϕ_P is the polymer volume fraction and v_p and v_s are the molar volumes of the polymer and the solvent, respectively. The first term represents the enthalpic contributions to the partial molar Gibbs free energy of mixing where χ_{PS} is the Flory–Huggins interaction parameter between the polymer and solvent. The second and third terms describe the entropic contribution.[49]

Equating the two equations leads to the following:

$$\ln\left(\frac{p}{p_{sat}}\right) = \frac{\mu_S - \mu_s^0}{k_B T} = \chi_{PS}\phi_P{}^2 + \left(1 - \frac{v_S}{v_P}\right)\phi_P + \ln(1 - \phi_P), \quad (4)$$

In one-dimensional solvent swelling of polymer films, the polymer volume fraction can be calculated as a ratio of a dry and solvent–swollen film thickness (*i.e.*, d_0/d, the inverse of the swelling ratio, SR). For typical solvent–polymer systems $v_p \gg v_s$, the linear term is approximated and eqn (4) can be recast in the following form:[50,51]

$$\ln\left(\frac{p}{p_{sat}}\right) = \chi_{PS}\left(\frac{d_0}{d}\right)^2 + \frac{d_0}{d} + \ln\left(1 - \frac{d_0}{d}\right). \quad (5)$$

The analysis of film swelling provides a valuable experimental tool for determining the Flory–Huggins interaction parameter and information about solvent quality.[51–53] As shown in Fig. 2, the parameter can be evaluated from the slope of the difference between the log of p/p_{sat} and the entropic contribution plotted *versus* φ^2. Due to the concentration dependence of χ_{PS}, this relationship is linear only over a limited concentration range and in good solvents the polymer–solvent interaction parameter decreases with increasing polymer concentration.[51,53] For a given polymer, the parameter decreases in the order of increased preferential interactions with a solvent. For example, for polybutadiene $\chi_{PB\text{-ethanol}} = 3.41$, $\chi_{PS\text{-acetone}} = 1.64$, $\chi_{PS\text{-butyl acetate}} = 0.52$, and $\chi_{PB\text{-toluene}} = 0.14$.[54] The interaction parameter can assume negative values indicating strong attracting interaction between polymer and solvent.[55]

In addition to the chemical interactions, polymer swelling behavior is dictated by the degree of solvent vapor saturation in the gas phase, which in turn is affected by the temperature. polymer–solvent swelling equilibria are highly sensitive to changes in ambient temperature due to the exponential dependence of

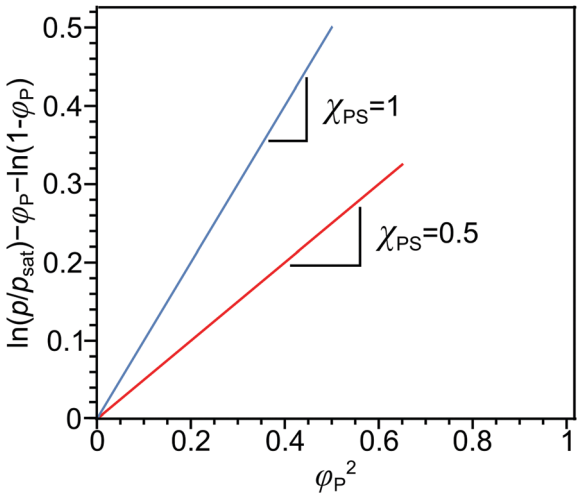

Fig. 2 Evaluation of polymer–solvent interaction parameter from 1D solvent swelling. Plots of the differences between the log of solvent partial pressure and the entropic contribution *versus* the square of polymer concentration for χ_{PS} = 1 (blue line) and χ_{PS} = 0.5 (red line).

the vapor pressure on the temperature given by the Clausius–Clapeyron thermodynamics relation: $p \sim p_0 \exp(-\Delta H/RT + \text{const})$, where ΔH is the specific enthalpy of vaporization. Frequently, saturated vapor pressure at a given temperature range is calculated using the empirical Antoine equation:

$$\log_{10}(p_{sat}) = A - [B/(C + T)], \quad (6)$$

with A, B, C constant values available for majority of common solvents.[56,57] It is worth noting that reaching or exceeding the saturation vapor pressure or operating below the dew point temperature leads to solvent condensation and uncontrollable swelling, and dissolution of the polymer film usually accompanied by its delamination.

Solubility parameter and the Flory–Huggins interaction parameter

A comparison of the solubility parameters (δ) can be conveniently use to evaluate the quality of solvent towards a particular polymer instead of χ_{PS} determination. The solubility parameters theory developed by Scatchard, Hildebrand and Scott introduces square root of the cohesive energy density to be a quantitative metrics for estimating the solvency of a particular solvent:

$$\delta = \left(\frac{\Delta H_{vap} - RT}{v_S}\right)^{1/2} \quad (7)$$

where v_s is the molar volume of the solvent and ΔH_{vap} is the heat of vaporization.[58] The Hildebrand–Scatchard equation relates the difference between the solubility parameters of the polymer (δ_P) and solvent (δ_S), and the enthalpy of mixing:

$$\Delta H_{mix} = \varphi_P \varphi_S v_M (\delta_P - \delta_S)^2, \quad (8)$$

where v_M is the molar volume of the mixture, $v_M = x_P v_P + x_S v_S$.[59]

Solubility analysis was subsequently developed by Hansen, who introduced partial contributions to the solubility parameter originating from hydrogen-bonding (δ_H), polar (δ_P), and nonpolar dispersive interactions (δ_D), which effectively map the parameter in a three-dimensional space and allow analysis of more complex solvency scenarios.[59]

$$\delta^2 = \delta_D^2 + \delta_P^2 + \delta_H^2 \quad (9)$$

The contributing terms to the solubility parameters for various compounds are tabulated[59] or can be calculated, *e.g.*, by the group-contribution method proposed by Stefanis and Panayiotou.[60]

Finally, the Flory–Huggins interaction parameter and solution parameters are interrelated through the Hildebrand–Scatchard regular solution theory:[61]

$$\chi_{P-S} = \chi_H + \chi_S = \frac{v_m}{RT}(\delta_P - \delta_S)^2 + 0.34, \quad (10)$$

where χ_H – enthalpic contribution factor, χ_S – entropic contribution factor, δ_i – Hansen solubility parameter for each component. The constant term adds a contribution resulting from the entropic effects. For non-polar systems, 0.34 is a commonly used correction attributed to the entropic factors.[46] For block copolymers and polymer blends the χ-parameter is calculated for each polymer–solvent pair.[46,48,59]

Dry BCP morphologies

In BCP melts, the spontaneous microphase separation begins at the order–disorder transition temperature (T_{ODT}) and, in the case of BCP solutions, above a critical polymer concentration (φ_{ODT}). The transition is driven by chemical dissimilarity between the polymer chains and leads to the formation of nanoscale morphologies consisting of distinct domains. In BCP melts, the entropic term can be neglected and the chemical incompatibility between blocks is expressed as:

$$\chi_{A-B} = \frac{v_0}{RT}(\delta_A - \delta_B)^2, \quad (11)$$

where χ_{A-B} is the Flory–Huggins polymer–polymer interaction parameter and v_o is the geometric mean of the BCP segments molar volumes, $v_0 = [v_A M_A v_B M_B]^{0.5}$, where v and M are the monomer volume and molecular weight, respectively.[62] The interaction parameter quantifies the degree of chemical dissimilarity between the blocks and thus the strength of microphase separation. For example, for symmetric diblock BCPs, the limiting value of the product of χ-parameter and the degree of polymerization N at the T_{ODT} is given by:[63,64]

$$(\chi N)_{ODT} \sim \frac{1}{T_{ODT}} = 10.5, \quad (12)$$

Typically, the as-cast BCP films are trapped in a metastable glassy state with highly disordered or very poorly developed domains. This state persists as long as the material remains below the glass transition temperature, T_g, above which the chains' mobility is sufficiently increased, and phase separation occurs. BCP chains of similar type aggregate with each other, separating from the dissimilar block chains, and form domains. This initial rapid local ordering is later superseded by a much slower grain growth, *i.e.*, the process of morphology coarsening

over larger length scales known as grain growth. As outlined in the last section of this review, BCP coarsening proceeds *via* diffusion of structural defects and their annihilation and, in particular, in high molecular weight BCP melts, this process can be exceedingly slow and the demanded degree of order could never arise. Hence, numerous BCP annealing strategies known as directed self-assembly methods, have been developed. They offer both kinetic control, frequently accelerating BCP grain growth kinetics by several-fold compared to the standard thermal annealing, and structural control by utilizing directional biases which drive the formation of certain morphologies and align them. Such orienting biases include the electric,[65,66] magnetic,[67,68] thermal gradients,[69,70] or shear-fields[71,72] and their use in BCP patterning can be found in several excellent review publications.[4,7,8,10,16]

In the microphase-separated state, the volume ratio of the blocks and the interfacial energy minimization principles define the geometric shape of BCP domains. Typically encountered morphologies include cubically-packed spheres, hexagonally-packed cylinders, gyroidal networks, and lamellae. The interaction parameter determines the strength of the segregation and affects the degree of chain stretching at the interface between the blocks, and the width of the composition gradient, $w \sim \frac{2a}{\sqrt{\chi}}$, where a is the statistical segment length.[73] It is step-like in the strong-segregation limit (SSL) in high-χ systems and broadens to the width of entire domain, assuming a sinusoidal profile in the weak segregation limit (WSL).[63] The characteristic repeat spacing, L (BCP periodicity) scales with the degree of BCP polymerization as: $N^{2/3}$ for $\chi N > 29$ (SSL); $N^{1/2}$ for $\chi N < 5$ (WSL, near the onset of chain stretching), and as $N^{0.83}$ for intermediate-segregation regime.[74]

Morphologies of BCP films in the presence of solvent

The presence of neutral solvent reduces chemical incompatibility between the BCP blocks and decreases the effective interaction parameter χ_{eff} according to the dilution approximation:[75,76]

$$\chi_{\text{eff}} \sim \phi_{\text{P}}(\chi_{\text{AB}} + \Delta\chi) = \phi_{\text{P}}(\chi_{\text{AB}} + \chi_{\text{AS}} - \chi_{\text{BS}}) \qquad (13)$$

where ϕ_{P} is the volume fraction of the copolymer and $\Delta\chi$ is the difference between the solvent-block A and solvent-block B interaction parameters. For near-neutral solvents, the $\Delta\chi$ term can be neglected and χ_{eff} is simply proportional to the BCP concentration:

$$\chi_{\text{eff}} \sim \phi_{\text{P}}\chi_{\text{AB}} \qquad (14)$$

According to the modified dilution approximation, χ_{eff} scaling is steeper: $\chi_{\text{eff}} \sim \chi_{\text{AB}}\phi^{\beta}$ with the scaling exponent β assuming values 1.3–1.6.[77,78] The non-selective solvent induces a decrease in segregation strength marked by a vertical downwards trajectory (A) on a BCP phase diagram depicted in Fig. 3a. This decrease results in thermodynamically-preferable mixing when a critical BCP concentration is reached, effectively lowering the order–disorder transition temperature ($\chi_{\text{ODT}} \sim 1/T_{\text{ODT}} \sim \varphi_{\text{BCP}}{}^{-\beta}$).

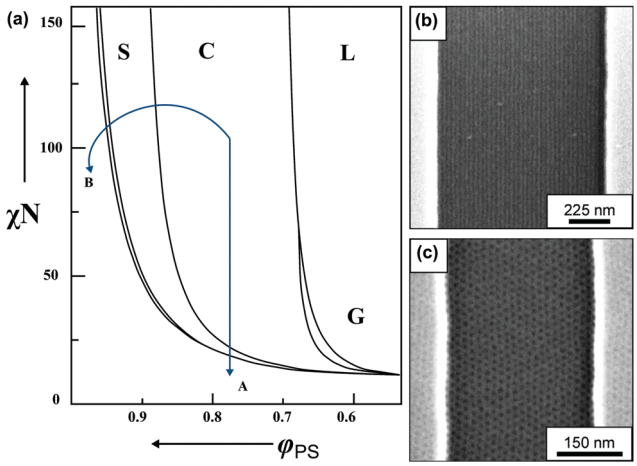

Fig. 3 BCP morphology transitions in the presence of solvent. (a) Schematic BCP phase diagram with swelling trajectories in a non-selective solvent – A and block-A selective solvent – B. Distinct morphologies marked as L – lamellae, C – cylinders, S – spheres, G – gyroid, DIS – disordered. (b) Solvent-induced morphology transitions of cylinder-forming PαMS-*b*-PHOST in topographic trench pattern. Horizontally aligned cylinders after annealing in non-selective solvent – THF. (c) Hexagonally-packed spheres pattern annealed in acetone vapors (PHOST-selective solvent). (a) Adapted with permission from *Macromolecules*, **43**, 2463.[80] Copyright 2010 American Chemical Society. (b and c) Adapted with permission from *ACS Nano*, **2**, 1396.[81] Copyright 2008 American Chemical Society.

The solvent-driven ODT for a given BCP–solvent system starts when $\chi_{\text{eff}}N$ reaches the critical value.

For block-selective solvents the dependence of the effective Flory–Huggins parameter on BCP concentration can be more complex. The effective value of χ_{AB} in a selective solvent is given by:[73,79]

$$\chi_{\text{eff}} = \frac{(\chi_{\text{AS}} - \chi_{\text{BS}})^2}{(\delta_{\text{A}} + \delta_{\text{B}} - 2\delta_{\text{S}})^2}\frac{RT}{v} \qquad (15)$$

The preferential swelling scenario results from a large difference between χ_{AS} and χ_{BS}. In the limiting case of a strongly-preferential solvent which swells just the block A, its volume fraction, ϕ_{A} increases to:

$$\phi_{\text{A}} = 1 - \phi_{\text{AB}}(1 - \phi_{\text{Adry}}) = 1 - \phi_{\text{AB}}\phi_{\text{Bdry}}, \qquad (16)$$

where ϕ_{AB} is the concentration of the swollen BCP and ϕ_{Adry} and ϕ_{Bdry} are volume fractions of the blocks in the dry state. Selective swelling shifts the morphology position diagonally on the BCP equilibrium diagram (trajectory B in Fig. 3a).

In the presence of a strongly selective solvent, the effective interaction parameter between the polymer blocks might be increased, inducing microphase separation of an initially disordered system, or a shift from a weakly- to strongly segregated material. This opens an interesting possibility for solid-state transformations of BCP morphology by post-casting chemical processing[82] which improves the structural parameters (*e.g.*, lowers the line-edge roughness) relevant for BCP patterning applications.

In addition to the morphological transitions described above, the presence of solvent induces rearrangements of BCP chain conformation and affects the characteristic repeat-spacing, L (d-spacing, periodicity). Neutral solvent screening of unfavorable enthalpic interactions between the blocks relaxes chain conformation at the block interface. According to the mean-field theory prediction, the repeat spacing, L, in a semi-dilute BCP solution is given by the power law:[83]

$$L \sim \phi^{\beta} \tag{17}$$

with $\beta \approx 0.22$ for strongly-segregated systems. Experimentally measured scaling exponents vary from 0.23 to 0.33 for non-selective and from -0.51 (period dilation) to 0.46 for selective solvents, as thoroughly discussed by Zhang *et al.*[84] The contraction of characteristic spacing of BCP morphology in a near-neutral solvent can equivalently be considered to be driven by the reduction in the effective χ parameter:[85]

$$L \sim \chi_{\mathrm{eff}}^{\frac{1}{6}} \sim \phi^{\frac{\beta}{6}} \chi_{\mathrm{AB}} \tag{18}$$

The degree of period contraction or dilation and its evolution in solvent-augmented annealing of BCP thin films also depend strongly on the interaction with the substrate, orientation of the domains with respect to the solvent diffusion front, film thickness, and the annealing trajectory including deswelling ramps.[84,86–90] In selective solvents complex swelling behavior involving several period-scaling regimes, morphology transitions, and domain reorientation have been reported.[84,91–93]

Kinetic effects

The presence of the solvent has a pronounced effect on chains' mobility and reduces the glass transition temperature T_g of glass-forming polymers. The T_g of a solvent–swollen polymer can be estimated using the empirical Fox formula:[94]

$$\frac{1}{T_g} = \frac{w_P}{T_{gP}} + \frac{w_S}{T_{gS}}, \tag{19}$$

where T_{gP}, T_{gS} and w_P, w_S are the glass transition temperatures and weight fractions of a polymer and a solvent, respectively. Significant reduction of T_g in the presence of solvent allows structural rearrangements and ordering of otherwise glassy block copolymers at room temperature.

Polymer chains diffusion coefficient is accelerated in the presence of solvent in accordance with: $\langle D \rangle \sim D_0 \exp^{-\gamma N \chi_{\mathrm{eff}}}$, where D_0 is the self-diffusion coefficient in a hypothetical phase-mixed system and γ is a constant ($\gamma \approx 1$). In asymmetric diblocks $N = N_A$, the number of segments of the minority block.[42,95]

The rearrangement of BCP morphology by chains' diffusion across the domain interface is given by an activated mechanism, strongly enhanced by reduction of χ_{eff} in the presence of a neutral solvent:[42,96]

$$D_{\mathrm{per}} = D_0 \exp[-\gamma N_A(\chi_{\mathrm{eff}} - \chi_{\mathrm{ODT}})], \tag{20}$$

where D_0 is the translational Rouse's diffusivity of a homopolymer of the matching degree of polymerization (N) at the same temperature, $D_0 = k_B T/N\xi_r$, with ξ_r, the monomer friction coefficient.[96] In BCP melts the diffusivity parallel to the block interface, D_{par}, is 10^3–10^4 faster than the perpendicular diffusivity, D_{per}, and can be approximated by D_0.[97] The degree of solvent saturation strongly affects the characteristic time of phase segregation, reducing it by several orders-of-magnitude compared to the dry-state annealing.[42]

BCP thin-film casting

Block copolymer thin films ($d < 1000$ nm) are almost exclusively prepared by casting, *i.e.*, the deposition of a polymer solution onto solid substrates followed by the evaporation of the solvent. Spin-coating (spin-casting, SC), flow-coating (blade-coating, FC), and dip-coating (DC) are popular BCP casting methods with spin-coating arguably the most widespread because of its robustness and compatibility with integrated circuits (IC) fabrication. A simple spin-coater consists of a rotary chuck to which a solid substrate is affixed, driven by a motor at a regulated rotational speed (1000–6000 RPM). The consecutive steps of a film casting are presented in Fig. 4a. After placement of a controlled volume of polymer solution on a substrate, the chuck is accelerated to a constant rotational speed and the solution is spread over the substrate with the majority of the solution volume spun off over the edges by the inertial forces. Since 95–99% of the solution volume is lost in this step, it is perhaps the most significant drawback of this method, especially when used to deposit films made of valuable materials. The spin-off step takes about a few seconds depending on the acceleration ramp profile, target spin velocity, and polymer solution parameters such as density and viscosity; the evaporation of a solvent is negligible and the thickness of the film is reduced to a few micrometers.[98] During the second step, a balance of inertial and viscous forces is established, and a uniform wet film is formed on the substrate. In the last phase, the wet film thickness is reduced by solvent evaporation driven by the diffusion of the solvent towards the surface of the film until a dry film thickness is reached.[99] The wet film thickness is inversely proportional to the square root of rotational speed and the same scaling is preserved in dry films.[98,100] The method is highly reproducible, largely independent of polymer composition when casting is performed from the same solvent, and allows fine control of sample thickness and high coating uniformity. SC is compatible with fine topographic surface patterns used in graphoepitaxial DSA.[45,101] Nonetheless, the high-material-loss drawback and SC inability to provide films of variable thickness on a single substrate make other casting methods equally attractive in research.

In flow-coating (Fig. 4(b)), a polymer solution is spread over a substrate by a movable blade oriented almost horizontally with respect to the substrate surface.[102,103] This blade geometry and its proximity to the substrate provide a gap (50–300 μm high) in which a polymer solution is hosted by capillary forces and which acts as an "ink" reservoir during the solution-spreading. For spreading blade velocities typically used in FC (v = 1–50 mm s^{-1}) wet-film formation is governed by the

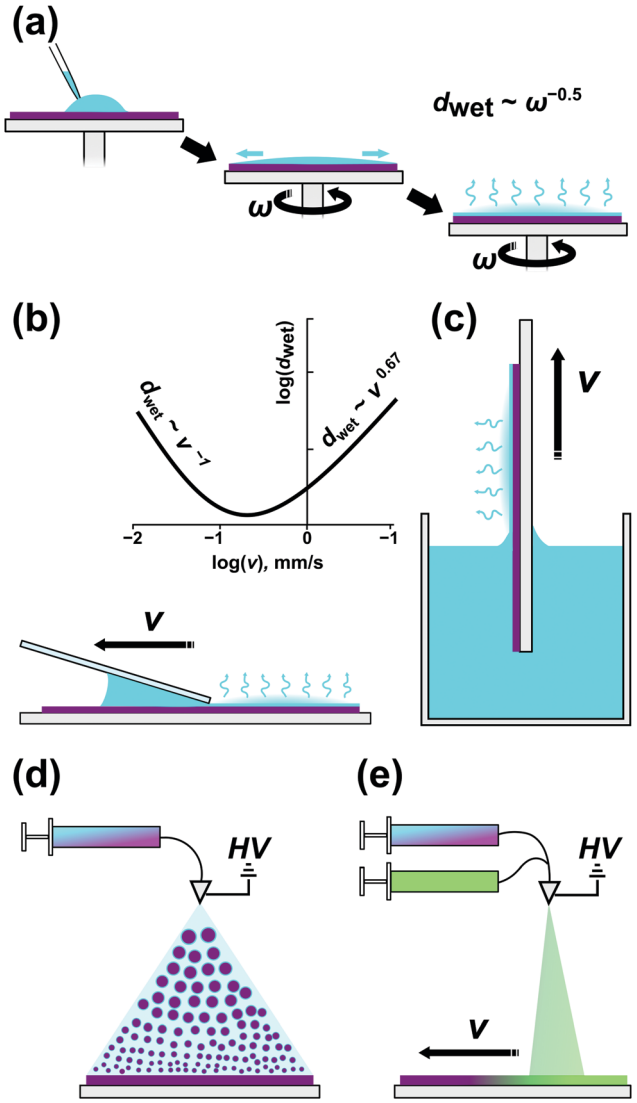

Fig. 4 BCP film casting methods. (a) Spin-coating. (b) Blade-coating. (c) Dip-coating. (d) Electrospray deposition of a polymer film with a homogeneous composition and (e) with a lateral composition gradient.

surface-tension-modified viscous flow, *i.e.*, the Landau–Levich flow problem,[104] in which the film thickness scales as $v^{2/3}$. Blade acceleration during the coating enables the formation of films with controlled thickness gradient.[103] Compared to SC, the amount of material wasted is significantly smaller and depends on the size of the coated substrate and the amount of solvent which must be retained in the gap to ensure coating uniformity. The highest yield (>95%) can be achieved with blade coaters incorporated in roll-to-roll deposition systems, which provide a continuous coating on large-area flexible substrates.[105,106] Consistent blade height and angle alignment, as well as edge cleanliness, affect the quality and reproducibility of the coated films.

In dip-coating, a solid substrate is immersed in a vessel filled with a BCP solution and withdrawn with a constant speed, dragging along a thin meniscus of evaporating liquid (Fig. 4(c)). The simplicity of this approach might be deceptive as several environmental factors affect the final layer thickness. In DC we distinguish two separate flow regimes – capillary and draining – that are dictated by a substrate withdrawal speed. As shown in Fig. 4b, in the Landau-Levich, viscous flow regime, d_{wet} scales as $v^{2/3}$ and as v^{-1} for the small-velocity, capillary regime.[107] Many processing parameters influence the final film morphology apart from the withdrawal speed – solvent volatility, BCP concentration, surface tension, and viscosity are of crucial importance.[108] DC, in contrast to SC, does not waste much material but at the same time requires the preparation of greater volume of the dipping solution. Simultaneous coating of both sides of a substrate can be advantageous in some applications, *e.g.*, deposition of antireflective coatings on transparent substrates.[109] It is worth noting that only dip-coating can be directly used for conformal substrate patterning of non-flat substrates including fibers and corrugated surfaces.[110,111]

A recently introduced BCP coating method – the electrospray deposition (ESD), relies on formation of a fine jet of BCP-containing droplets atomized by high voltage applied to a conductive nozzle (Fig. 4(d)). The ESD process exploits the microphase separation of BCP in the droplets as solvent evaporates *en route* to a heated substrate and can be thought of as a macromolecular CVD analog allowing epitaxial growth of ordered BCP layers.[112] Despite the initial instrument construction and set-up efforts, ESD offers unique capabilities of controlling film morphology gradients in the direction normal to substrate surface and in the lateral direction. For example, such composition gradients can be realized by controlling the proportion of two BCP solutions fed into the spraying cone during the vertical growth or while moving the substrate laterally (Fig. 4(e)).[112,113] Similarly, high voltage-driven flow was utilized by Onses *et al.* in electrohydrodynamic (EHD) near-field jet printing of BCP patterns with complex geometry and remarkable sub-500 nm lateral resolution.[114] The technique can be used for precise BCP ink deposition on grapho- and chemoepitaxially patterned surfaces allowing hierarchical BCP ordering.[115] In terms of material usage, both ESD and EHD jet printing are material-saving techniques. In ESD the losses are generated mostly at the periphery of the deposition zone where the coating is uneven.

While spin-coaters are readily available commercially and there are a few vendors offering dip-coaters, the other coating systems are typically home-built and their construction requires custom hardware and certain integration skills.

The selection of the casting method and the casting solvent may influence the morphology of the BCP in the subsequent annealing step. For example, casting of poly(styrene-*b*-dimethylsiloxane) (PS-*b*-PDMS) from PDMS-selective solvent resulted in horizontal cylinders and shifted to hexagonally perforated lamellae and horizontal lamellae when solvent solubility parameter was increased.[116] Casting solvent can also affect the ordering kinetics; for PS-*b*-PDMS it has been shown that less-volatile solvents providing less free volume results in higher degree of order in the subsequent SVA annealing.[117] In some cases, the magnitude of residual stresses present in the glassy BCP after the casting, could determine the final orientation of BCP morphology.[118,119]

Review of solvent-assisted self-assembly of BCP films

For the sake of systematic presentation, we divided the solvothermal annealing methods into three categories depending on when BCP ordering takes place, *i.e.*, ordering simultaneous with casting (direct casting), post-casting ordering, and a separate, hybrid methods category in which two or more ordering biases are used, typically after the casting step.

Simultaneous casting and annealing methods

We first review direct casting methods as, historically, slow evaporation of concentrated solutions was one of the first methods to obtain ordered bulk BCP specimens for microscopic imaging and X-ray scattering experiments.[120,121] The existence of ordered morphologies in non-preferential solvents above the order–disorder transition concentration ($\varphi_{BCP} > \varphi_{ODT}$), reflecting that of dry neat BCP material has been predicted theoretically and well-documented experimentally.[83,87] Slow evaporation of a solvent from a concentrated BCP solution has been shown to yield well-ordered morphologies.[122–124] Notably, a suitable selection of the casting solvent and ambient atmosphere conditions can lead to vertically ordered BCP morphologies aligned by the solvent evaporation front.[125–127]

BCP-evaporating solvent interactions can be leveraged to control macroscopic orientation of domains in deposited thin films. Kowalewski *et al.* utilized the zone casting process, originally developed for obtaining large-area arrays of small molecule single-crystals[128] in which BCP solution is cast from a slit-shaped nozzle onto a slowly moving substrate (Fig. 5(a)).[129] By adjusting the temperature of the substrate the authors aligned cylindrical PODMA-*b*-PtBA-*b*-PODMA (poly(octadecyl methacrylate)-*b*-poly-(*t*-butyl acrylate)-*b*-poly(octadecyl methacrylate)) triblock parallel or perpendicular to the deposition direction indicating the role of crystalline block in the selection of alignment direction.[130]

Direct casting in the presence of selective solvent has also been used to obtain well-ordered vertical arrays of BCP cylinders including poly(styrene-*b*-ethylene oxide) (PS-*b*-PEO).[125] It is worth noting that direct casting and controlled evaporation of solvent is a widespread method for self-assembly of bottlebrush copolymers and block copolymers with record-high molecular weight ($M_n > 10^3$ kg mol^{-1}). The processing and use of these materials as photonic crystals has been thoroughly reviewed in a recent publication by Grubbs and coworkers.[23]

Non-solvent assisted casting methods. Initially used for casting homopolymer membranes,[132] the non-solvent induced phase separation (NIPS), was extended to BCP self-assembly (SNIPS).[133,134] In SNIPS, a concentrated BCP solution (10–25 wt%) cast on a substrate is immersed into a non-solvent bath inducing a non-equilibrium propagation of morphology-ordering solvent front (Fig. 5(d–f)).[135,136] This effect was demonstrated for cylindrical poly(styrene-*b*-4-vinylpyridine) (PS-*b*-P4VP) cast from dimethylformamide (DMF) and DMF/tetrahydrofuran (THF)/dioxane mixtures followed by immersion in water[135,137–139] This method can be used with other amphiphilic BCP systems, *e.g.*, poly(styrene-*b*-*N*,*N*-dimethylaminoethyl methacrylate), to create pH- and temperature-responsive membranes, as presented by Schacher *et al.* who demonstrated the formation of self-supporting defect-free films significantly exceeding 100 μm^2 using 75 kg mol^{-1} BCP.[140] The SNIPS-process is used in fabrication of ultrafiltration membranes for water treatment.[141,142]

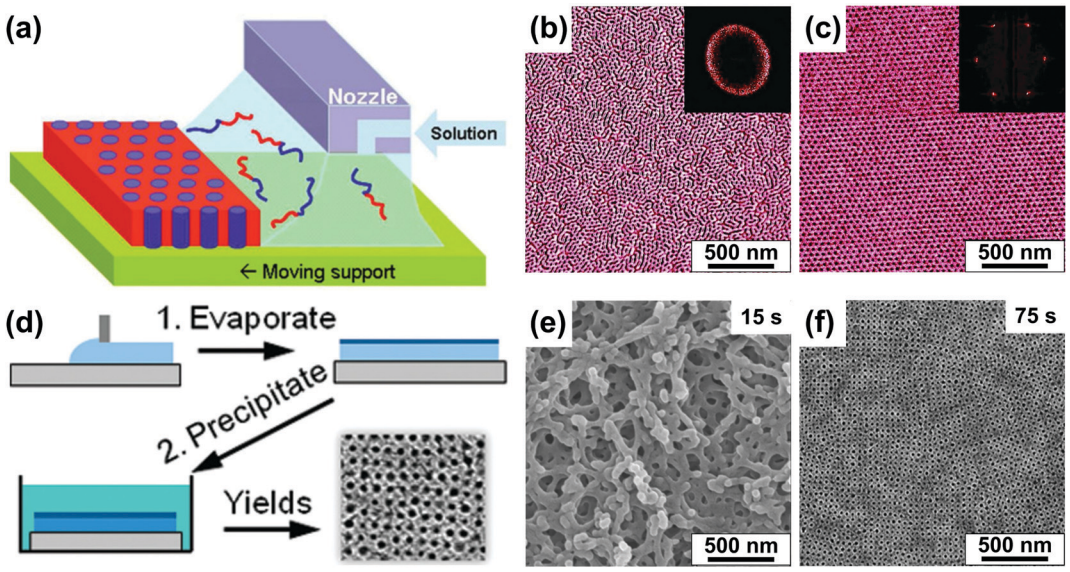

Fig. 5 Direct casting methods. (a) Schematic representation of the zone casting technique utilizing a slit nozzle to deliver BCP solution to a moving substrate. (b and c) AFM images of PS-*b*-PB BCP films produced at different printing speed (b) 500 μm s^{-1} and (c) 2 μm s^{-1}. (d) Schematic of preparation of a porous BCP membrane with SNIPS. (e and f) SEM images of poly(isoprene-*b*-styrene-*b*-4-vinylpyridine) films precipitated after (e) 15 s and (f) 75 s of volatile solvent evaporation. (a-c) Adapted with permission from *J. Am. Chem. Soc.*, **133**, 11802.[129] Copyright 2011 American Chemical Society, (d–f) adapted with permission from *Nano Lett.*, **11**, 2892.[131] Copyright 2011 American Chemical Society.

A detailed review of this subject was published by Phillip *et al.*[143] and recently by Yang *et al.*[144]

Crystallization induced alignment. A special case of a morphology-directing bias field induced by surface interactions has been proposed by Thomas and coworkers who utilized directional crystallization of BCP solvents–benzoic acid or anthracene to guide the orientation of lamellar and cylindrical poly(styrene-*b*-methyl methacrylate) (PS-*b*-PMMA) and poly(styrene-*b*-isoprene) (PS-*b*-PI) diblocks.[145]

Ordering in slowly-evaporating solvents. Volatility of the casting solvent has a significant impact on the rate of evaporation that takes place in the second stage of casting (see Section 3 for details). During this stage, the BCP concentration increases and, at the critical BCP concentration (φ_{ODT}), the system undergoes an order–disorder transition into a microphase-separated state. For a typical BCP casting protocol using $\approx$1 wt% polymer solution in volatile solvents such as toluene, propylene glycol methyl ether acetate (PGMEA), or THF the whole casting process is accomplished within 30–60 s and the residence time between the φ_{ODT} and the concentration at which the polymer undergoes a glass transition and vitrifies is very short ($\sim$1 s). Therefore, the effective ordering duration is very limited and the resulting as-cast films are disordered or present only very poorly-developed morphology, resembling micellar state at the onset of ODT. To extend the ordering step, solvent evaporation can be slowed down by introducing low vapor-pressure solvents. Jung *et al.* demonstrated the ordering of PS-*b*-PMMA by spin-casting, from high boiling point, diphenyl and dibenzyl ethers while introducing simultaneous IR heating to facilitate solvent evaporation.[146] The authors observed well-ordered lamellar structures for polymers with M_n ranging from 51 to 235 kg mol^{-1} (Fig. 6(a and b)). More recently, Weller *et al.* developed a method called non-volatile solvent vapor annealing (NVASA)[147] relying on the addition of non-volatile solvents (dibutyl phthalate for PS-*b*-PEO and chloronaphthalene for poly(styrene-*b*-2-vinylpyridine (PS-*b*-P2VP)) to the BCP-casting solution in a volatile host solvent (toluene). The amount of non-volatile additives controls the plateau thickness of the film during the last stage of drying and affects the final BCP morphology. In the case of dibutyl phthalate used for annealing PS-*b*-PEO, the non-volatile plasticizer has to be removed from a film by immersion in ethanol (Fig. 6(c–e)). A similar approach was used by Leniart *et al.* who investigated the formation of long-range ordered horizontal patterns of cylindrical PS-*b*-P2VP cast from a mixture of toluene and non-volatile di- and trimethoxytoluene in a process called solvent evaporation annealing (SEA).[40] The proper solvent selection of the casting mixture composition and solvent evaporation rate enables the formation of grains of controllable size in a single casting step performed with a spin-coater as a sole processing tool (Fig. 6(f–h)). Further investigations of the SEA mechanism revealed that a relatively narrow concentration window, just above the φ_{ODT} ($0.33 < \varphi < 0.40$) facilitates rapid coarsening of BCP grains with the later drying stage inconsequential for the formation of large grains.[148] This result indicates

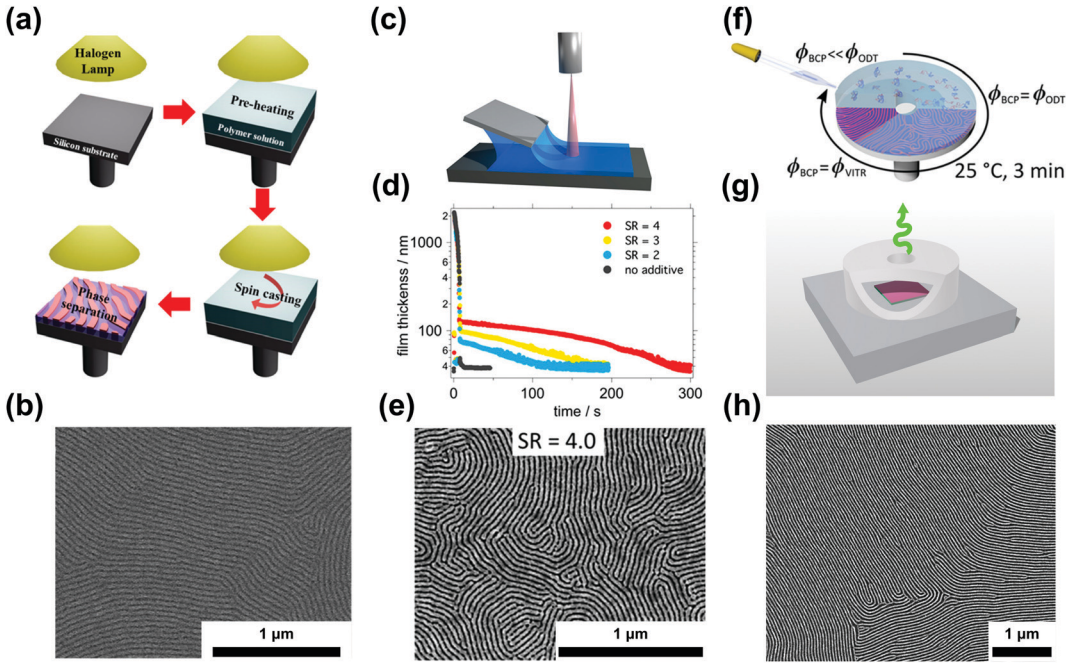

Fig. 6 Ordering in slowly-evaporating nonvolatile solvents. (a) Schematic representation of a single-step casting assisted by halogen lamp heating and (b) the resulting ordered PS-*b*-PMMA film. (c) Blade coating setup used in nonvolatile additive solvent annealing (NVASA). (d) Film thickness evolution during the drying process at different swelling ratios and (e) SEM image of PS-*b*-P2VP ordered at SR = 4. (f) Schematic representation of solvent evaporation annealing (SEA) during spin-coating and with a convection-limiting cap (g) yielding large-grained BCP samples (h). (a and b) Adapted with permission from *ACS Macro Lett.*, **4**, 656.[146] Copyright 2015 American Chemical Society, (c–e) adapted with permission from *Macromolecules*, **52**, 5026.[147] Copyright 2019 American Chemical Society, (f–h) adapted with permission from *Macromolecules*, **53**, 11178.[40] Copyright 2020 American Chemical Society.

the importance of the early stages of BCP ordering and underscores the utility of BCP processing strategies in which the ODT transition is crossed and grains are nucleated from a disordered state, an approach exploited in other direct casting methods and some field-assisted DSA methods.[149,150]

Post-casting annealing

Solvent vapor annealing. Solvent vapor annealing is arguably one of the most effective and popular methods for ordering block copolymer thin films. Thanks to an almost unlimited choice of solvent or solvent mixtures that allow fine-tuning of polymer–solvent interactions, SVA has been successfully used in ordering BCP films of various chemical composition and diverse morphology, including diblock spheres (PS-*b*-PMMA,[151] PS-*b*-PDMS[117]), gyroidal networks (PS-*b*-PMMA[152]), cylinders (poly(styrene-*b*-lactic acid) (PS-*b*-PLA),[153] PS-*b*-PDMS,[154] PS-*b*-P2VP[155,156]), lamellae (PS-*b*-PLA,[157] PS-*b*-PMMA,[158,159] PS-*b*-PDMS[154]), and other block copolymers.[122,124,155,160–163] SVA has been comprehensively reviewed in excellent publications by Sinturel *et al.*[164] and more recently by Jin *et al.*[165] Since SVA is frequently a method of choice for scientists who are starting their work with BCP thin films thanks to a relatively low entry barrier in terms of equipment complexity and price, we would like to discuss the experimental details of this technique.

The popularity of SVA led to the rapid development of dedicated BCP processing protocols and instruments, shown schematically in Fig. 7. Starting from static annealing in a glass desiccator or a metal dish filled with a liquid solvent (Fig. 7(a)),[166,167] SVA setups progressively evolved towards more advanced systems that offer a higher degree of process control. In addition to precisely thermostated annealing chamber,[88] SVA setups include a separately thermostated solvent vapor saturator (bubbler)[42,168] and a set of flow regulators and gas mixers[84] which control the degree of solvent vapor saturation in a stream of carrier gas introduced to the chamber. Due to the steep dependence of saturation pressure on temperature, a tight control of temperature is critical to avoid solvent condensation. For this reason, in advanced SVA experiments, the temperature of the introduced solvent vapor, and the annealing chamber, is properly adjusted with a PID-controlled heating stage.[42]

Most laboratory setups are equipped with an optical attachment for real-time monitoring of the film swelling process. Even a simple optical microscope with a color camera can be used to qualitatively assess the solvent uptake by the film, by tracking the evolution of interference color patterns and detecting usually undesirable film dewetting or surface reconstruction. Quantitative measurements of the swelling ratio, *i.e.*, the ratio of the solvent–swollen and dry film thicknesses are realized by white light spectral reflectometry (WLSR)[154,173,178] or spectral ellipsometry (SE).[179–182] While both techniques are very robust, the former is more affordable and enables faster measurements and therefore is more popular. Nonetheless, precise thickness determination with WLSR is difficult when the exact value of the effective refractive index of the swollen film is unknown or difficult to compute without additional insights into its composition, *e.g.*, annealing in a mixture of two or more solvents. In such cases, iterative approach to WLSR data analysis or SE can be employed.[176] Alternatively, an *in situ* quartz chemical microbalance (QCM),[183] or an AFM measurement[184] can be used to monitor the degree of polymer swelling. In particular, *in situ* AFM is an exclusive technique that provides real-time and real-space insights into the evolution of the morphology of native BCPs, and can be used to track the BCP grain coarsening in SVA.[184–187]

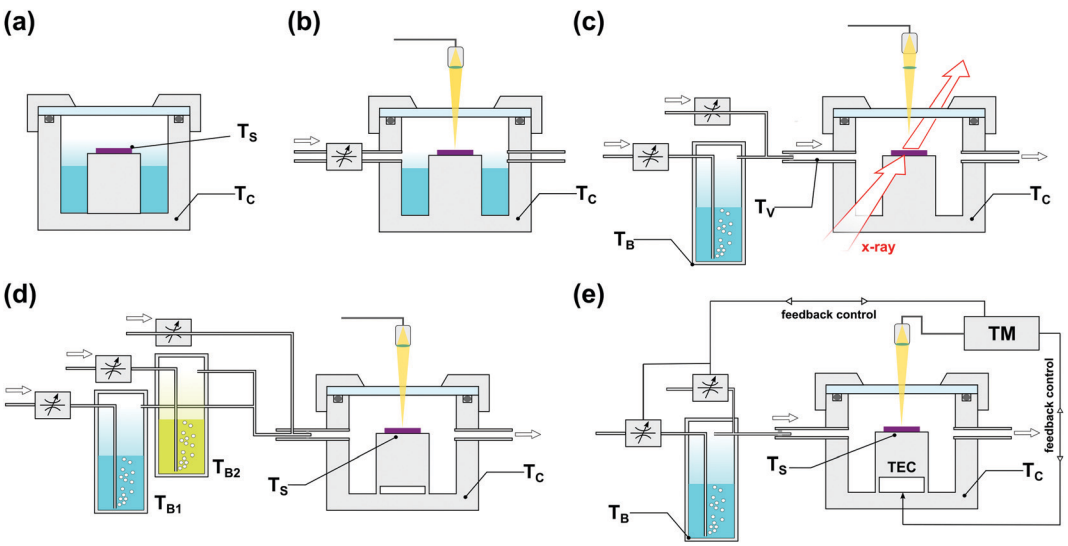

Fig. 7 Commonly employed solvent vapor annealing apparatus. (a) Static chamber.[81,158,159,169] (b) Flow setup with solvent saturation controlled by an inflow of inert gas with solvent reservoir inside the chamber and optical thickness monitor.[117,124,170–174] (c) Flow setup with external solvent vapor saturator and gas mixer compatible with *in situ* GISAXS measurements.[87,93,156,175] (d) Double bubbler setup with gas mixer for experiments with controlled composition of binary solvent vapor mixture.[154] (e) High precision setup with automated closed-loop SR control by temperature differential[176] or vapor composition[177] adjustment.

The *in situ* grazing-incidence small angle X-ray scattering (GISAXS) is a particularly suitable tool for monitoring the progress of SVA.[93,156,171,175,188] This non-invasive technique can be integrated with most SVA experiments (Fig. 7(c)) providing information on the morphological transitions in the film including the domains' orientation and the extent of long-range order.[87,163,175,180,188–190] The in-depth profiles of solvent concentration distribution in the swollen film can be inferred from X-ray[175] or neutron[191] reflectometry studies.

Special care must be taken when reporting and comparing the results of SVA. In particular, the reported "duration of annealing" depends whether the authors define this parameter as the overall processing duration, *i.e.*, time spent in SVA chamber or as a time of effective exposure to a vapor at certain degree of saturation. As pointed out by Tang *et al.*, the apparent time-scales of BCP ordering in static SVA depend on the chamber volume.[127] The authors modeled the 1D transport of solvent vapor in the chamber with the second Fick's law of diffusion with appropriate initial and boundary conditions:

$$\frac{\partial c_S}{\partial t} = D_S \frac{\partial^2 c_S}{\partial z^2}; \quad c_{S(0,t)} = c_{S,sat}; \quad \frac{dc_S}{dz}_{(z=L)} = 0, \qquad (21)$$

where $C_s(t, z)$ is the concentration and D_s is the diffusivity of solvent vapor in the gas phase, and z is the vertical distance measured from the meniscus of a liquid solvent. They concluded that, despite the local equilibrium concentration of the solvent in the film is established very quickly, reaching the steady vapor concentration in the entire chamber can take up to several hours.[127] An analogous effect has been reported by Jeong *et al.*, who used a solvent-infused PDMS pad placed in proximity of a BCP film to significantly shorten the annealing time in epitaxial trench patterns (5 s *vs.* ~10 h in a static chamber).[192]

Long swelling ramps in the static chamber SVA extend the overall processing time and contribute to BCP ordering in a difficult-to-control manner. Similarly, the deswelling ramps frequently affect the end-point morphologies and cannot be precisely controlled.[124,193] For a tight control of these ramps, more advanced SVA setups are required. In a flow chamber, modeled as continuously-stirred tank reactor, the characteristic residence time, τ, given by the volume-to-flow ratio, defines the time necessary to establish steady-state vapor saturation after the vapor delivery is started. The time needed to achieve 90% and 99% of the final saturation is 2.3τ and 4.6τ, respectively. It can be reduced by using a small-volume chamber or by increasing the flow rate, the latter associated with a potential risk of decreasing the solvent vapor saturation degree by shortening the residence of carrier gas in the bubbler. For the outlined reasons, recently reported advanced SVA setups include a separate control of the saturation degree (by adjustable temperature and flow through the bubbler) and are thermostated independently in several places including the gas mixer, vapor delivery tubing, chamber walls, and a sample post (Fig. 7(d and e)).[42,168,177] Fully-automated experiments with control of solvent-uptake and desorption ramps are enabled by a closed-loop regulation of the gas flow control of vapor saturation ratio with a real-time feedback from the thickness monitor (Fig. 7(e)).[153] Alternatively, this approach is also very effective in the flow setups; as proposed by Hulkkonen *et al.* the temperature differential between the introduced solvent vapor and BCP sample can be used to affect the swelling ratio offering very fast SR response (Fig. 8).[176] The setup offers a high degree of SR setpoint accuracy through a PID control of the process and enables non-trivial swelling ramps such as sine or triangular waves suitable for testing intriguing concepts of order enhancement in BCP thin films by cyclic annealing.[194]

Due to the strong enhancement of polymer chain dynamics in the presence of a solvent, SVA emerged as a particularly potent tool for ordering ultrahigh molecular weight BCPs (M_n > 500 kg mol^{-1}). These materials pose a great challenge for other DSA methods due to their prohibitively slow grain-coarsening kinetics. Such BCP materials can generate patterns with periods larger than 100 nm, extending the BCP applications to large-period plasmonic coatings, and photonic band-gap materials.[13,18,23,195]

A two-step solvothermal annealing has been first demonstrated as an efficient way to order lamellar PS-*b*-PMMA (256 kg mol^{-1}, unguided self-assembly) and M_n = 733 and 1000 kg mol^{-1} epitaxially guided patterns by Kim *et al.*[159] Recent reports on homologous materials include successful production of microporous ultrafiltration gyroidal membrane obtained by selective etching of PS-*b*-PMMA (M_n > 600 kg mol^{-1}).[196] Real-time AFM observation of highly-swollen (SR ≈ 9) 1000 kg mol^{-1} lamellar PS-*b*-PMMA grain-coarsening has been reported by Takano *et al.*[184] Doerk *et al.* presented a remarkable example of SVA efficiency combined with low molecular weight homopolymer blending by ordering ultra-high M_n PS-*b*-PMMA (M_n = 2000 kg mol^{-1}) and obtaining patterns with L_0 > 200 nm (Fig. 9(a)).[174] SVA is also effective in large M_n high segregation strength BCP systems including PS-*b*-PVP homologs. Cummins *et al.* indicated the importance of solvent neutrality and the underlayer brush for ordering vertical PS-*b*-P2VP lamellae (M_n = 429 kg mol^{-1}) in the presence of PGMEA vapors.[197] SVA performed at a high swelling ratio has been demonstrated by Selkirk *et al.* to efficiently order PS-*b*-P2VP lamellae of 800 kg mol^{-1} (Fig. 9(b)).[177] The importance of high-degree of swelling in annealing of high-χ materials is corroborated by an earlier report identifying a narrow solvent saturation window ($0.94 < p/p_{sat} < 1$) to be effective in ordering PS-*b*-P4VP cylinders (M_n = 34 kg mol^{-1}). This trend is corroborated by an *in situ* GISAXS-SVA study performed by Gu and coworkers who observed formation of large-grained lamellar PS-*b*-P2VP grains in the vicinity of the solvent-driven ODT.[198]

Solvent selectivity is a dominating factor determining morphology selection in SVA.[117,154,167,199] Solvent vapor composition coupled with the appropriate film thickness have been demonstrated to induce the transitions of native BCP structure into a range of non-native morphologies (Fig. 10).[167,200] Wu *et al.* reported kinetic transformations of PS-*b*-PLA from an initially disordered state, through cylindrical state towards native thermodynamically-defined gyroidal morphology dependent on solvent

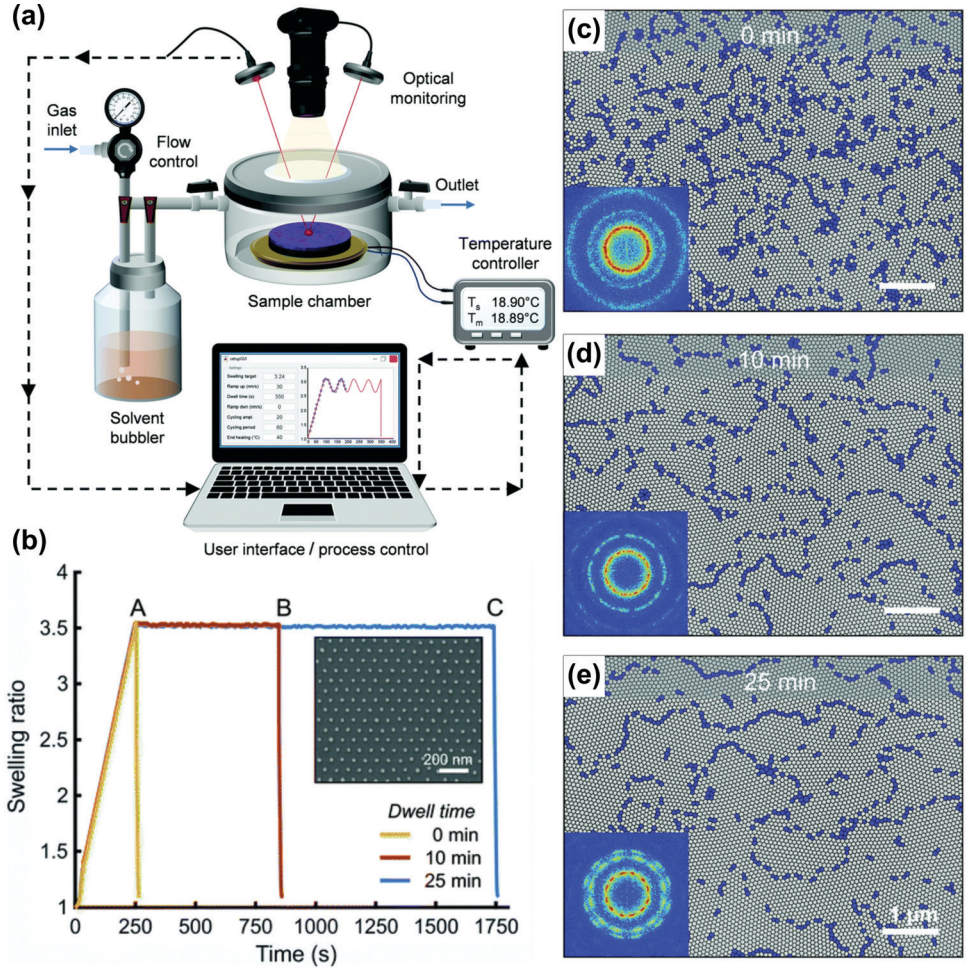

Fig. 8 Automated solvent vapor annealing. (a) Schematic of an advanced SVA setup with closed-loop SR control. (b) Annealing pathways of cylinder-forming PS-*b*-P2VP 258 kg mol^{-1} thin films in THF vapor and corresponding morphologies after 0, 10, and 25 min (c–e). Adapted from *Soft Matter*, **15**, 7909.[176] With permission from The Royal Society of Chemistry.

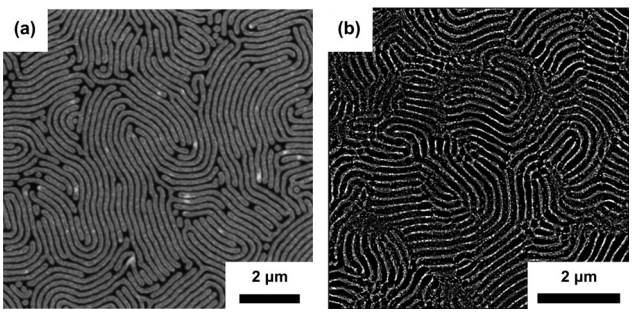

Fig. 9 SVA of large-periodicity block copolymer systems. (a) SEM image of a blend of 1051 kg mol^{-1} and 2000 kg mol^{-1} PS-*b*-PMMA with 3 kg mol^{-1} PS and 3 kg mol^{-1} PMMA homopolymers obtained after consecutive SVA in THF and hot-plate thermal annealing ($L_0 \sim 211$ nm). (b) SEM image of PS-*b*-P2VP (793 kg mol^{-1}) annealed in THF-chloroform mixture ($L_0 \sim 180$ nm). (a) Adapted with permission from *Macromolecules*, **53**, 1098.[174] Copyright 2020 American Chemical Society, (b) adapted with permission from *Macromolecules*, **54**, 1203.[177] Copyright 2021 American Chemical Society.

removal rate.[201] Similar intricate ordering phenomena were demonstrated for other diblocks, *e.g.*, PS-*b*-P2VP,[202] PS-*b*-P4VP,[86,203] PS-*b*-PMMA[204,205] or PS-*b*-PDMS[90,206,207] and triblocks.[208]

SVA and BCP multilayers

Fast ordering kinetics render SVA as a particularly useful high-throughput method advantageous in multi-step assembly of complex BCP architectures. Jung *et al.* utilized SVA-assistance for ordering of PS-*b*-PDMS to produce 2D and 3D silica nanomesh patterns.[209] Homologous material has been used in the iterative coating-SVA-etching approach by Cheng *et al.* to engineer hierarchical superhydrophobic multilayered SiO_2 coatings.[210] Non-native multilayered ZnO structures were fabricated by templated synthesis using solvent vapor annealing as a rapid ordering method of BCP templates.[211,212]

Combinatorial exploration of SVA

Finding suitable SVA conditions and engineering the optimal processing pathway remain a challenge and require systematic studies. Combinatorial experiments offer a great promise in this regard and have been applied to elucidate SVA phenomena, e.g., screening for optimal solvent-mixture composition in gradient-composition solvent vapor annealing[178] and in recent autonomous investigations of film thickness effects.[213]

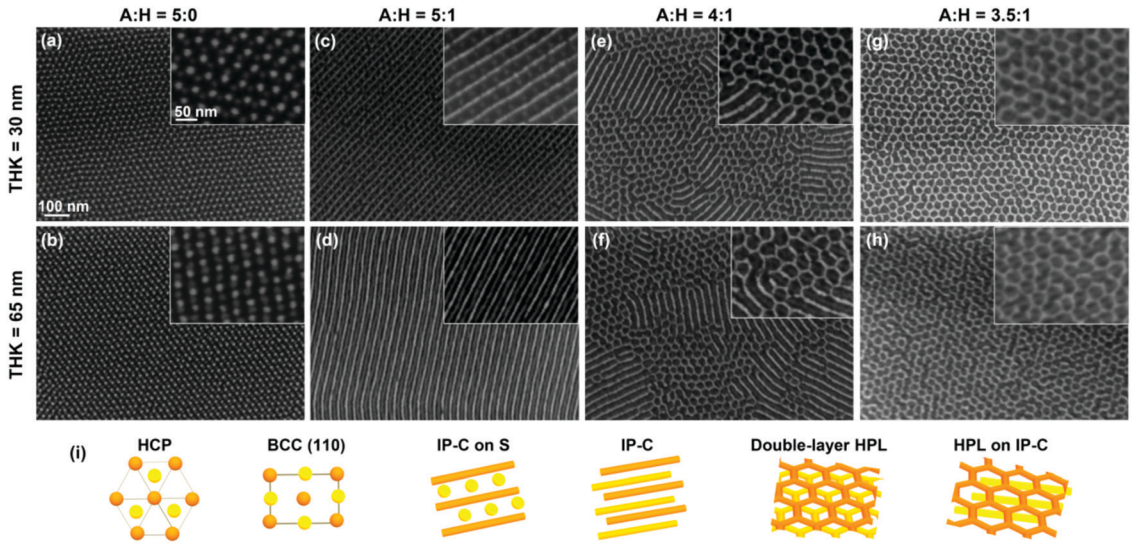

Fig. 10 Morphology evolution for PDMS-*b*-PS-*b*-PMPCS terpolymer of different film thickness exposed to vapors of acetone:heptane mixture of various composition. The bottom row depicts models of the above layered morphologies. Reprinted with permission from *ACS Macro Lett.*, **8**, 852.[200] Copyright 2019 American Chemical Society.

Raster solvent vapor annealing. An interesting modification of SVA method, raster solvent vapor annealing (RSVA) enabling local control of BCP morphology, has been proposed by Epps and coworkers. They used a circular nozzle 0.2–0.5 mm in diameter to locally deliver THF vapor to swell and order cylindrical poly(styrene-*b*-isoprene-*b*-styrene).[214] The width of uniformly ordered zone depends on the solvent delivery parameters and can be controlled by, *e.g.*, nozzle diameter, nozzle-to-polymer distance, however, the diffusive mechanism of solvent delivery, broadens the transition between the patterned and unpatterned regions. As discussed in Section 4.3.2, the RSVA method can be coupled to soft-shearing to induce BCP morphology alignment.

Warm solvent vapor annealing and high-pressure SVA. Significant increase of defect annihilation kinetics and shortening of time required to order cylindrical PS-*b*-PDMS annealing in graphoepitaxial trench pattern with warm (40–60 °C) solvent vapor compared to a control experiment performed at room temperature has been demonstrated by Kim *et al.*[215] Solvothermal approach has been used by Morris and coworkers in processing PS-*b*-PLA in the presence of warm THF vapors.[157] Researchers from the same group performed a microwave-assisted SVA study indicating a key role of polar THF molecules as radiation-absorbers facilitating heat-transfer and rapid self-assembly.[216] The efficiency of microwave solvothermal annealing, can be further enhanced by coupling it with graphoepitaxy[217] and by simultaneously increasing the temperature and pressure of the SVA process. The latter approach was proposed by Buriak and coworkers who obtained remarkably long-range ordered PS-*b*-PMMA and PS-*b*-P2VP by SVA in sealed microwave reactors using THF or toluene with peak-pressure reaching 8 bar and temperature up to 160 °C, exceeding the normal boiling point of these solvents.[218,219]

Immersion annealing (IA). The concept of annealing of BCP thin films by immersion in a liquid solvent is very similar to SVA; polymer–solvent swelling equilibrium is governed by equation analogous to eqn (2). Compared to SVA, IA is perhaps easier to realize and control experimentally, and requires optimization of only two parameters – the temperature and composition of the immersion bath. Park *et al.* reported rapid (<5 min) immersion-induced self-assembly of cylindrical PS-*b*-PDMS guided by graphoepitaxial patterns swollen by a mixture of toluene (PS-selective) or/and ethanol (a non-solvent). IA has been shown to be effective in unguided ordering of PS-*b*-PMMA and PS-*b*-P2VP by Modi *et al.*[105] Recently, a multi-step combination of solvent vapor and IA has been proposed by Choi and coworkers to induce rapid morphological transformations in sphere-forming PS-*b*-PDMS diblock.[207] The relative insensitivity of DIA to the fluctuations of the ambient conditions as compared to SVA and its compatibility with the roll-to-roll fabrication render DIA a very compelling DSA tool. DIA can be utilized both for reproducible BCP patterning and for quantitative investigations of self-assembly, *e.g.*, grain coarsening studies or polymer swelling in ternary solvent mixtures, difficult to investigate using SVA.[73]

Hybrid methods

Solvent-assisted BCP annealing can be coupled with other DSA methods to further increase the ordering efficiency and to introduce morphology-aligning biases. In this section, we discuss experimental reports which utilize such hybrid processing strategies.

Solvent-assisted BCP epitaxy. Epitaxial ordering utilizes topographic reliefs (Fig. 11) or chemically functionalized surface patterns to laterally guide the orientation of BCP domains. Epitaxy has been demonstrated to significantly shorten the time needed for self-assembly, at the same time reducing pattern defectivity. The phenomenon underlying the enhanced ordering is the commensurability between symmetry and size of epitaxial

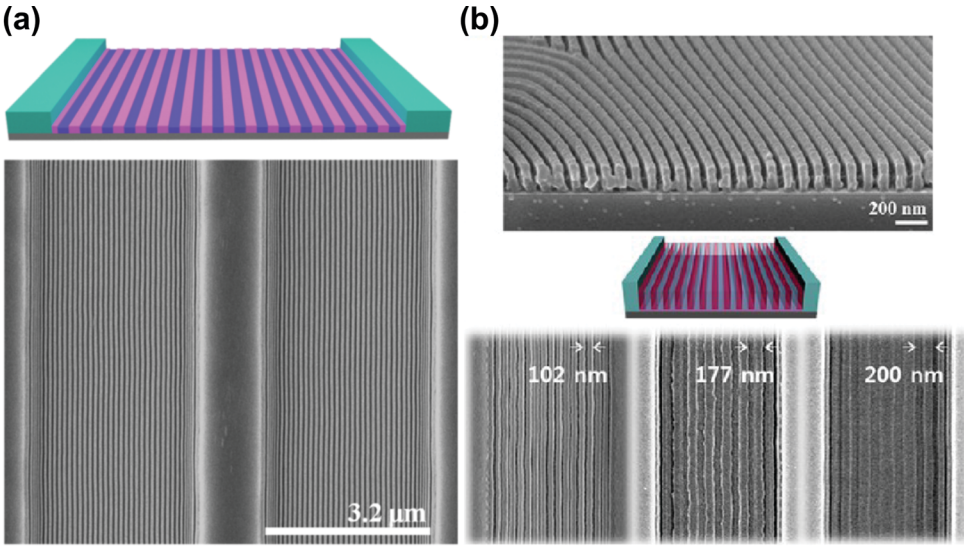

Fig. 11 Solvent vapor-assisted graphoepitaxial ordering of high MW PS-*b*-PMMA lamellar patterns. SEM images of films in trench confinement. (a) 3.2 μm wide trench; (b) cross-section view and top-down images of 1.5 μm wide trench. Reprinted with permission from *Macromolecules*, **49**, 1722,[88] and *ACS Nano*, **7**, 1952.[159] Copyright 2016, 2013 American Chemical Society.

ordering pattern and BCP lattice.[89,220–224] A comprehensive review of the topic has been published by Ji[225] and Gunkel.[9] Here, we provide a short review of solvent-assisted epitaxial patterning as an important extension of SVA.

As opposed to thermal annealing, solvent–vapor processing is usually performed at room temperature. This advantage is particularly important in annealing materials prone to thermal degradation such as BCP lithographic photoresists as pointed out by Bosworth *et al.* who combined graphoepitaxy with SVA to order PαMS-*b*-PHOST patterns.[81] Choi *et al.* showed the dependence between the choice of an ordering method (SVA or TA) and the final orientation of cylinders in shallow topographic patterns.[45] SVA-assisted graphoepitaxy has been extensively investigated by Ross and coworkers who demonstrated successful alignment of BCP morphologies such as line and hexagonally-packed dot patterns of high-χ PS-*b*-PDMS materials for use in high resolution lithography.[226–228] This approach also proved successful in the self-assembly of non-native BCP motifs such as square lattices,[229] mixed morphologies[154] or concentric circles and spiral patterns.[230] SVA-graphoepitaxy combination has also been applied to other copolymer systems including, multiblock,[163,231] bottlebrush,[232] and liquid crystalline BCPs.[233,234]

Chemical epitaxy (or chemo-epitaxy) utilizes preferential wetting interactions between chemically patterned surfaces and distinct BCP blocks. Chemo-epitaxial ordering is frequently coupled with thermal annealing,[225] nevertheless, several reports of SVA-assisted chemical epitaxy have been published including studies exploiting an important BCP-lithography concept of improving patterning resolution by density multiplication,[172,235] and formation of non-equilibrium morphologies.[236] Aligned multilayered metallic nanomesh templated by BCPs were produced by SVA-assisted grapho- and chemoepitaxial ordering. This multistep ordering is driven by two distinct interactions – trench wall guidance of the first layer and edge nucleation of the upper layer.[237]

SVA of BCPs in rigid confinement. Solvent vapor-induced ordering of soft materials confined in nanoporous templates (SAINT) made of anodic aluminum oxide (AAO) has been demonstrated as a compelling method for templating 3D BCP structures with various morphologies.[238,239] An interplay between surface wetting effects and selective swelling of amphiphilic BCP domains in the binary mixture of two solvent vapors has been exploited to tune the morphology of PS-*b*-PEO diblock confined in porous template.[240] More information on the formation of 3D polymer structures, especially in anodic aluminum oxide (AAO) templates, can be found in the recent comprehensive review by Ok *et al.*[241]

Solvent-induced soft shearing. The application of tangential mechanical stress transduced by an elastomeric PDMS pad to an underlying BCP film has been originally proposed by Angelescu *et al.* as an effective way of aligning BCP morphologies.[71,242] Large thermal expansion coefficient of PDMS, compared to the film substrate, results in BCP soft-shearing during the local thermal and photothermal annealing and can be used for the same purpose.[243–245] Analogously, the differential expansion of the PDMS cap in the presence of solvent vapor in SVA induces soft-shear and lateral orientation of BCP. This approach has been proposed and investigated in detail by Qiang *et al.* for a large group of BCPs including PS-*b*-PI-*b*-PS, PS-*b*-PB-*b*-PS, PS-*b*-P2VP, PS-*b*-PDMS both in general radial pad expansion[246] and uniaxial expansion scenarios.[247] Local solvent vapor delivery and PDMS swelling in soft shear-RSVA has been reported to guide the alignment of triblock PS-*b*-PI-*b*-PS cylinders; conversely, rapid, large-area macroscopic patterning can be realized with the use of slit-shaped nozzle.[248] SVA-SS already served as a processing method in a synthesis of conductive carbon[249] and layered silica mesh.[250] Shelton *et al.*

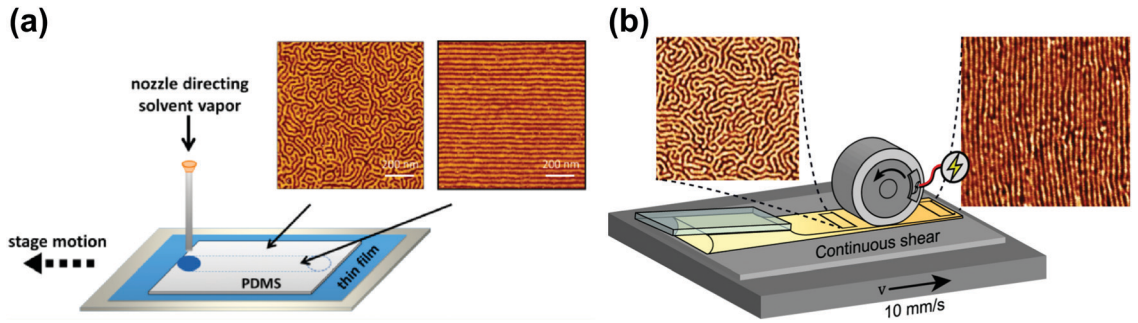

Fig. 12 Soft-shear SVA. (a) Raster SVA soft-shearing. AFM morphologies of horizontally oriented PS-*b*-PI-*b*-PS cylinders after fast (left) and slow (right) vapor rastering; (b) scheme of an inline rolling shear alignment (IRSA) setup consisting of casting and shearing roller elements PS-*b*-PI-*b*-PS forming cylinders. AFM morphologies before (left) and after (right) the passage of the shearing roller. Reprinted with permission from *ACS Macro Lett.*, **4**, 516,[248] and *ACS Appl. Polym. Mater.*, **4**, 682.[255] Copyright 2015 and 2021 American Chemical Society.

performed SANS study of SVA-SS ordering kinetics with special attention to swelling and deswelling stage and its beneficial or detrimental influence on grain coarsening.[251] Zhang *et al.* investigated the SVA-SS ordering for thicker films up to 100 μm.[44] Sung *et al.* utilized SVA-SS effect to obtain perpendicularly ordered lamellar domains of high-χ fluorinated star block copolymer.[252] SVA-SS ordering effect was exploited by Kang *et al.* for a fabrication of Au plasmonic nanostructures.[253] An interesting two-step combination of soft-shearing, followed by a SVA treatment method presented by Kim *et al.*, led to exquisite effects in terms of scalability of good quality alignment.[254] Recent advance combining both SVA and soft-shearing benefits in a single roll-to-roll setup was proposed by Epps and coworkers (Fig. 12(b)).[255]

Solvent-assisted laser annealing. Photothermal annealing has been successfully used for ordering and guiding BCP morphologies.[10] Although high-intensity large-area illumination can enhance evaporation and induce self-assembly BCP during casting from non-volatile solvents,[146] in typical volatile solvent BCP annealing this approach could be counter-productive, leading to instantaneous solvent evaporation. This drawback has been overcome by Singer *et al.* who used microscope setup in focused laser spike (FLaSk) zone annealing, to induce directional fusion and alignment of solvent–swollen PS-*b*-PDMS micelles in a direct-write fashion.[256] Among the non-epitaxial solvent-assisted BCP patterning method, with the width of a patterned zone $\approx$1 μm, FLaSK offers the highest degree of spatial control.

Residual solvent effects in thermal annealing

The presence of residual solvent, *i.e.*, the solvent entrapped in polymer films after the casting, can be detected by spectroscopic methods, X-ray and neutron reflectometry (NR),[191] and gas chromatography-mass spectrometry.[257–259] The exact amounts of residual solvent reported in literature vary from less than 2 vol%[260] to more than 10 vol%.[261] They seem to depend on several factors including the chemical nature of polymer, its molecular weight, film thickness and the presence of underlying brush layers, and the casting method. It is certainly difficult to measure a minute loss of solvent from the film and the discrepancies in literature reports could also be a result of differences in measurement resolution, data quality, and data analysis protocols.[260] It is worth noting that upon thorough drying of glassy polymers below the T_g, the solvent is replaced by voids.[182] Interestingly, the presence of this rather insignificant amount of residual solvent is clearly accelerating BCP ordering kinetics. A quantitative grain-coarsening kinetic studies reported by Ferrarese-Lupi *et al.* have shown that the trapped solvent accelerates the early stage ($<$100 s) of coarsening of lamellar PS-*b*-PMMA domains by increasing the kinetic exponent.[257,261] This quantitative assessment of the residual solvent effects was possible by applying rapid thermal processing (RTP) furnace which allows fast access to high annealing temperatures without prior removal of the solvent, whose concentration, according to Perego *et al.*, decreases towards the substrate surface.[261] Seguini with coworkers demonstrated appearance of two coexisting morphologies in RTP-treated BCP films – vertical cylinders in a solvent-rich region and periodic lamellar structures on a solvent-depleted polymer/air interface.[258,259] The reservoir of solvent is provided by the random block copolymer (RCP) brush layer beneath the BCP used to promote vertical orientation of BCP domains. In general, higher amount of trapped solvent was responsible for faster grain-coarsening kinetics.[258] Recently, Sparnacci *et al.* provided an insightful analysis of solvent distribution in RCP/BCP systems using NR.[262]

Residual solvent clearly plays an important role in BCP self-assembly but can be obscured by more pronounced effects such as shear- and confinement ordering, therefore a consistent sample preparation protocol is of crucial importance in quantitative BCP self-assembly studies. Special care must be taken to either thoroughly remove the entrapped solvent (*e.g.*, by vacuum desiccation), especially when its presence could be detrimental[263] or to use it to one's benefit.

Grain-growth kinetics in solvent-assisted BCP self-assembly

Grain coarsening, *i.e.*, the development of long-range orientational and positional order in block copolymer thin films under annealing is the longest stage of their morphological evolution and frequently a bottleneck of the patterning process.[264]

Overcoming this problem has strongly motivated research aiming at the development of DSA methods that shorten the time required to produce a BCP morphology with minimal density of structural defects or, alternatively, the largest grain-size.[254,265–268] Due to the enhancement of chain mobility discussed in Section 2, solvent-assisted DSA methods are particularly efficient in terms of accelerating grain-growth kinetics and defects annihilation rate, especially when compared to conventional thermal annealing, and can shorten the annealing time by several orders of magnitude.[28,42]

Quantitatively, the average BCP grain-size is computed from SEM or AFM images of BCP thin films or TEM section micrographs and reported as the in-plane domain orientation correlation length (ξ). This is done by a two-step process in which, first, a local domains' orientation is mapped, and then it is used to compute the orientational correlation function $g(r)$:[269]

$$g(r) = \cos[2(\varphi(\vec{r}) - \varphi(\vec{r}'))] \quad (22)$$

where, φ is the azimuthal angle of the local morphology orientation, r and r' denote the position vectors of the correlation pairs. The correlation is calculated for all possible separation distances (r) and averaged. The correlation function of a non-aligned BCP morphology calculated for a sufficiently large image follows an exponential decay:[222,270]

$$g(r) = \mathrm{e}^{-r/\xi_0} \quad (23)$$

with the ξ_0 a characteristic decay length, *i.e.*, $g(\xi_0) = e^{-1}$ reported as grain-size. The analysis can be performed for the horizontal cylinders or vertically-aligned lamellae (line patterns), hexagonally-ordered vertical cylinders, spheres or gyroidal morphologies, after accounting for a proper symmetry of the system. Contrary to real-space imaging, usually performed on dry films, X-ray scattering usually conducted in grazing-incidence or transmission geometry provides valuable real-time insights into the BCP ordering process.[173,175,198,271–273] While the azimuthal distribution of the scattering is used to track the reorganization of BCP domains orientation, the width of diffraction peaks carries information on the average grain-size (ξ). Scattering peak broadening in reciprocal space is evaluated using the Scherrer formula:[274]

$$\xi_{\text{X-ray}} = \frac{K\lambda}{\Delta(2\theta)\cos\theta} \quad (24)$$

where K is a shape factor, λ is the wavelength of the X-ray, Δ is a full-width at half-maximum (FWHM) of scattering peak, and θ is the Bragg diffraction angle. The limiting factor of the Scherrer approach is the broadening of scattering peaks due to instrumental resolution resulting in difficulties in large grains measurements. Conversely, morphological defects other than finite – grain-size effects contribute to peak broadening in this otherwise robust and versatile measurement technique. However, the X-ray scattering is not the only method that enables observation *in situ* of grain-coarsening – a proper AFM setup can be used alternatively.[184]

BCP grain coarsening process in constant-temperature thermal annealing is frequently described by an empirical kinetics power-law:[185,275]

$$\xi = At^{\alpha} \quad (25)$$

where $A = \frac{A_0}{\tau^{\alpha}} \cdot \mathrm{e}^{-\frac{\alpha E_a}{RT}}$ is the Arrhenius dependent term with E_a equal to the activation energy barrier for rate-limiting defect annihilation mode, and τ is the characteristic time of the order of microphase separation time-scales. The value of kinetic power-law exponent, α, depends on system dimensionality and topological constrains;[269] for line patterns it is equal to 0.25 for 2D patterns,[43,185,266,276–280] and $\approx$0.5–1 for 3D systems.[265,281] Nonetheless, experimentally-reported exponents, could be much lower, especially for lamellar patterns at longer annealing times.[97,257,280] Conversely, under non-stationary growth conditions, *e.g.*, rapid thermal processing,[282] presence of thermal gradients,[69,283] residual solvent effects,[257,261] or ordering under solvent evaporation,[40] higher scaling exponents were observed.

Eqn (25) is valid strictly under isothermal conditions and otherwise the quantitative grain-coarsening model becomes more complex. For analysis of grain-coarsening during slow heating ramps Fernandez-Regulez *et al.* proposed an approach, in which the non-isothermal annealing is divided into short quasi-isothermal intervals.[284] For each growth interval the preexisting grain size ξ_0, $\xi_0 = A(T)t_{eq}^{\alpha}$ is related to the equivalent annealing time, t_{eq}, used to translate the current growth curve to a next thermal interval step ($\xi = A(T)(t + t_{eq})^{\alpha}$). The computation is iterated until final temperature is reached. The model accounts for the linear variation of the pre-exponential factor and kinetic exponent with temperature: $\alpha = \alpha_0 + \alpha \cdot T$.

In solvothermal annealing, both A and α may, in principle, vary with temperature and solvent concentration, as well as other factors such spatial and temporal composition and temperature gradients. For this reason the quantitative kinetics data for solvent-assisted BCP coarsening are scarce, and frequently performed by scattering experiments.[84,163,198] Notably, Modi *et al.* presented kinetic studies of DIA process performed at a constant, moderate swelling ratio (SR = 1.6) of PS-*b*-PMMA,[105] reporting power law exponents at optimal ordering conditions was $\alpha = 0.27$, and the activation energy $E_a \approx 111 \pm 63$ kJ mol^{-1}, which is lower than observed in the thermal annealing processes (270 kJ mol^{-1}).[97] Very high value of apparent kinetic exponents $\alpha = 0.5$ was reported in SEA coarsening of cylindrical PS-*b*-P2VP in a series of controlled drying-time experiments,[40] which was the result of slow transition through ODT region, in which the ordering is the most efficient. The authors have reported $E_a = 26.9 \pm 2.7$ kJ mol^{-1}.

Recently, a semi-empirical kinetic model of grain coarsening in solvent assisted ordering under non-constant BCP concentration was proposed.[148] The kinetic exponent α has been found to exponentially decrease with the BCP concentration (φ):

$$\alpha(\varphi) = \alpha_0 \exp[-\chi N\varphi^{\beta}] \quad (26)$$

starting from $\alpha = 0.6$ near the ODT (SR $\approx$ 3) to $\alpha = 0.01$ (SR $\approx$ 2) for cylindrical PS-*b*-P2VP of 116 kg mol^{-1}. The dependence of

the effective kinetic exponent on solvent concentration resembles the exponential decrease of the thermal growth exponent with the BCP segregation strength (χN) reported by Seguini *et al.* in high-temperature annealing of cylindrical PS-*b*-PMMA homologs.[285]

Solvent-assisted grain coarsening pathways can be easily computed once the grain-coarsening rate map, *i.e.*, $d\xi/dt = f(\varphi, t)$ is determined from constant BCP concentration annealing experiments.[148] This approach, valid under a general assumption that instantaneous coarsening rate is only dependent on the current grain size and BCP concentration, is illustrated by Fig. 13a which shows two examples of grain-coarsening trajectories corresponding to SVA (green curve) and SEA (red curve) experiments mapped onto the φ–t space. The final grain size is calculated by numerical integration of the instantaneous rate along the distinct processing pathways (Fig. 13(b)). Equivalently, if the closed-form the grain size $\alpha(\varphi)$ and $A(\varphi)$ dependences are available, the rate equation:

$$\frac{d\xi}{dt} = A^{1/\alpha(\varphi)} \cdot \alpha(\varphi) \cdot \xi^{\frac{\alpha(\varphi)-1}{\alpha(\varphi)}} \quad (27)$$

derived from the power-law can be numerically integrated to yield $\xi(t)$. Even though this model was originally developed for solvent evaporation annealing, it can be easily used in quantitative analysis of other solvent-assisted DSA methods, *e.g.*, SEA if the precise information on swelling progress is availiable.[176]

In the case of very large-grained or aligned samples, the apparent correlation length $\xi = \infty$ due to the finite image-size or instrumental resolution limits. In such instances, direct defect counting methods or critical dimension analysis, *e.g.*, line edge roughness quantification are used to assess BCP pattern quality.[270,286,287] Such well-ordered BCP templates may still possess a small number of intrinsic defects, prohibitive to certain cutting-edge BCP applications such as IC patterning. A review article on the relevance of defect in BCP self-assembly has been published by Li and Muller.[288] This problem has been tackled theoretically, for various BCP chemistries and morphologies.[289–293]

Self-consistent field theory (SCFT) is a major simulation method harnessed for SVA-assisted BCP ordering and has gained a separate review in the topic.[294] In a simulation work of lamellar BCP Peters *et al.* calculated the defect annihilation rate for various segregation strength.[295] For higher values of a χN product combined with greater film thickness the defect healing rate drop is more pronounced. Xu *et al.* provided a number of valuable conclusions for SVA process for lamellar BCP.[296] The authors applied their model for the investigation of ordering dynamics for a non-selective solvent on substrates without chemical modification. In terms of defect removal rate they emphasized the role of initial film morphology on swelling dynamics that provides more uniform solvent distribution in the film volume which directly influences the annihilation rate. The outlined strategy for the efficient defect eradication consist of two steps – initially one makes defects labile by the excess uptake of solvent inside BCP volume which is then followed by a rapid solvent evaporation.

The kinetics of defects annihilation, as opposed to grain coarsening kinetics, can rarely be described by a simple power-law function, as it depends on the free energy of different types of defects, their relative mobility and annihilation mode.[186] The measure of defects density is especially useful in long-range orientationally ordered line patterns produced by epitaxial methods, in which dislocation or bridge defects are still present. Li *et al.* indicated pronounced differences in annihilation kinetics between certain types of defects, *e.g.*, the annihilation of dislocations follows power-law, annihilation of single periodicity bridges has no strong time-dependence, and annihilation of multiple periodicity bridges decreases exponentially with time.[268] Moreover, the higher temperature and lower thickness affect positively the defects annihilation. The defect density metrics of kinetics ordering has also been widely used as a quantitative tool to assess the efficiency of solvothermal BCP annealing including microwave-SVA.[216,218,219]

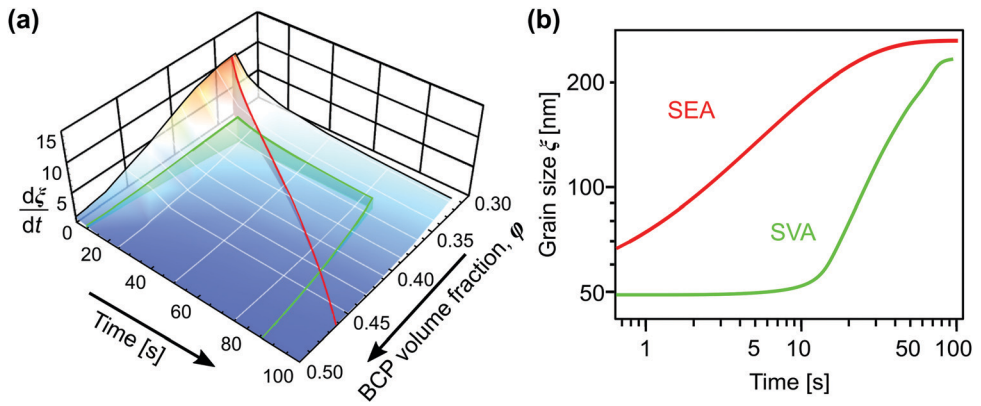

Fig. 13 (a) Trajectories of BCP processing in solvent evaporation annealing (red) with evaporation rate of 0.45 nm s^{-1} and solvent vapor annealing (green) with 5 nm s^{-1} swelling and deswelling ramps and 60 s dwell at constant film thickness (SR = 2.8). (b) Corresponding grain-coarsening curves predicted by the empirical model incorporating contribution from swelling and deswelling ramps. Adapted with permission from *ACS Macro Lett.*, **11**, 121.[148] Copyright 2022 American Chemical Society.

Conclusions and outlook

In this review, we have presented an overview of solvent-assisted block copolymer self-assembly phenomena and related DSA methods used in BCP surface patterning. These methods are an attractive alternative to other DSA techniques in terms of processing compatibility with multiple BCP materials of a broad molecular weight range, relatively low experimental complexity, and equipment cost. Despite the lack of consensus on which solvent-assisted DSA protocol provides the most satisfactory ordering results for a given BCP material, we cross-compared film deposition and annealing methods, indicating their advantages and drawbacks. We also reviewed quantitative tools used in the characterization of BCP morphologies and in the evaluation of the efficiency of BCP annealing protocols.

Although multiple solvent-assisted methods are very robust and reproducible, *e.g.* direct casting and solvent immersion annealing, the most widely used technique, solvent vapor annealing, and its derivatives seem to suffer from poor consistency of the reported results. We addressed this problem by analyzing the origins of experimental inconsistencies in SVA and indicated how the leading BCP research groups resolve them by properly designing their experiments. We believe that, among other factors, tighter control over swelling and deswelling ramps can greatly improve the consistency of SVA. This can be achieved by introducing a real-time monitoring of the swelling degree and a closed feedback loop to control this relevant parameter. In addition, *in situ* structural characterization methods such as GISAXS and AFM prove invaluable in elucidating solvent-induced BCP ordering mechanisms.

In our opinion, future advances in solvent-assisted BCP film patterning will develop in the following main directions. The first direction is dictated by the need for further research in the self-assembly of materials that cannot be treated with other DSA methods, such as ultrahigh molecular weight and temperature sensitive BCPs. The prospect of long-range ordering of the former BCP systems is particularly attractive for templating patterns with domain spacing commensurate with the wavelength of visible light exhibiting vibrantly colored Bragg diffraction. The second direction involves the development of robust methods of deposition of ordered BCP patterns on various substrates compatible with the high-throughput fabrication, *e.g.*, the roll-to-roll deposition or fiber coating. Here, we also underscore the future role of solvent-mediated annealing methods, which utilize additional ordering biases enabling uniaxial alignment and more complex BCP ordering scenarios. These hybrid ordering methods include epitaxy-coupled SVA for very precise local control of BCP patterns required in high-fidelity IC fabrication, deposition of multilayered systems from orthogonal solvents, and continuous shear alignment suitable for large-scale fabrication of macroscopically aligned BCP films. In our opinion, the exploration of this field holds great promise for practical utilization of BCP patterns. Finally, we predict the growing importance of solvent-mediated methods, which enable BCP morphology reconfiguration. In purely-thermal methods, an alteration (*e.g.*, reorientation of ordered lamellae) of the existing film morphology is very challenging requiring a strong reordering bias and taking a long time. On the contrary, solvent-driven phase transitions and BCP domain reorientation can be very rapid, enabling fast response to external stimuli. For numerous BCP systems, the introduction of a solvent is the only practical way of inducing the order–disorder transition since thermally driven ODT lies above their thermal damage threshold. Rapid ordering of BCP morphologies in proximity of the ODT is just one advantage of solvent-assisted DSA method, but, in our opinion, the ability of resetting, *i.e.*, reversibly bringing the ordered morphology to the consistent starting state, can be even more important for BCP self-assembly investigations. For instance, the reversible BCP self-assembly opens a fascinating perspective for autonomous *in situ* investigations of BCP film ordering carried out at synchrotron beamlines including optimization of processing conditions and kinetic studies performed on a single sample.

Abbreviations

BCP	Block copolymer
DSA	Directed self-assembly
FWHM	Full width at half-maximum
LC	Liquid crystal
ODT	Order–disorder transition
RCP	Random copolymer
RT	Room temperature
SCFT	Self-consistent field theory
SR	Swelling ratio
SSL	Strong segregation limit
WSL	Weak segregation limit

Materials

AAO	Aluminum anodic oxide
DMF	Dimethylformamide
P2VP	Poly(2-vinylpyridine)
P4VP	Poly(4-vinylpyridine)
PαMS	Poly(α-methylstyrene)
PB	Polybutadiene
PDMS	Polydimethylsiloxane
PEO	Polyethylene oxide
PGMEA	Propylene glycol methyl ether acetate
PHOST	Poly(4-hydroxystyrene)
PI	Polyisoprene
PLA	Poly(lactic acid)
PMMA	Poly(methyl methacrylate)
PODMA	Poly(octadecyl methacrylate)
PS	Polystyrene
P*t*BA	Poly(*t*-butyl acrylate)
THF	Tetrahydrofuran

Methods

AFM	Atomic force microscopy
BC	Blade-coating

CVD	Chemical vapor deposition
DC	Dip-coating
DIA	Direct immersion annealing
EHD	Electrohydrodynamic deposition
ESD	Electrospray deposition
FC	Flow-coating
FLaSK	Focused laser spike
GISAXS	Grazing-incidence small-angle X-ray scattering
IA	Immersion annealing
IC	Integrated circuit
NIPS	Non-solvent induced phase separation
NR	Neutron reflectivity
NVASA	Non-volatile solvent vapor annealing
QCM	Quartz chemical microbalance
RSVA-SS	Rapid solvent vapor annealing-soft shearing
RTP	Rapid thermal processing
SAINT	Solvent annealing induced nanowetting in templates
SC	Spin-coating
SE	Spectral ellipsometry
SEA	Solvent evaporation annealing
SEM	Scanning electron microscopy
SNIPS	Self-assembly non-solvent induced phase separation
SVA	Solvent vapor annealing
SVA-SS	Solvent vapor annealing-soft shearing
TA	Thermal annealing
WLSR	White light spectral reflectometry

Author contributions

All authors contributed to the writing of the manuscript. PP and AAL contributed equally to this work.

Conflicts of interest

There are no conflicts to declare.

Acknowledgements

AAL, PP, and PWM would like to acknowledge financial support from the First Team program (POIR.04.04.00-00-1DE6/16) of the Foundation for Polish Science co-financed by the European Union under the European Regional Development Fund. PWM also acknowledges a support received from the National Science Center, Poland, under the Sonata Bis grant agreement (2020/38/E/ST5/00328).

References

1 K. Ishizu and S. Uchida, *Prog. Polym. Sci.*, 1999, **24**, 1439–1480.
2 M. Hillmyer, *Curr. Opin. Solid State Mater. Sci.*, 1999, **4**, 559–564.
3 H. Feng, X. Lu, W. Wang, N.-G. Kang and J. W. Mays, *Polymers*, 2017, **9**, 494.
4 S. B. Darling, *Prog. Polym. Sci.*, 2007, **32**, 1152–1204.
5 I. W. Hamley, *Prog. Polym. Sci.*, 2009, **34**, 1161–1210.
6 H. C. Kim, S. M. Park, W. D. Hinsberg and I. R. Division, *Chem. Rev.*, 2010, **110**, 146–177.
7 M. Luo and T. H. Epps, *Macromolecules*, 2013, **46**, 7567–7579.
8 H. Hu, M. Gopinadhan and C. O. Osuji, *Soft Matter*, 2014, **10**, 3867–3889.
9 I. Gunkel, *Small*, 2018, **14**, 1802872.
10 S. R. Nowak and K. G. Yager, *Adv. Mater. Interfaces*, 2020, **7**, 1901679.
11 I. W. Hamley, *Angew. Chem., Int. Ed.*, 2003, **42**, 1692–1712.
12 F. H. Schacher, P. A. Rupar and I. Manners, *Angew. Chem., Int. Ed.*, 2012, **51**, 7898–7921.
13 M. Stefik, S. Guldin, S. Vignolini, U. Wiesner and U. Steiner, *Chem. Soc. Rev.*, 2015, **44**, 5076–5091.
14 C. Cummins, R. Lundy, J. J. Walsh, V. Ponsinet, G. Fleury and M. A. Morris, *Nano Today*, 2020, **35**, 100936.
15 C. Pinto-Gómez, F. Pérez-Murano, J. Bausells, L. G. Villanueva and M. Fernández-Regúlez, *Polymers*, 2020, **12**, 2432.
16 A. Subramanian, N. Tiwale, W.-I. Lee and C.-Y. Nam, *Front. Nanotechnology*, 2021, **3**, 766690.
17 S. Vignolini, N. A. Yufa, P. S. Cunha, S. Guldin, I. Rushkin, M. Stefik, K. Hur, U. Wiesner, J. J. Baumberg and U. Steiner, *Adv. Mater.*, 2012, **24**, OP23–OP27.
18 H. Hulkkonen, A. Sah and T. Niemi, *ACS Appl. Mater. Interfaces*, 2018, **10**, 42941–42947.
19 C. Kilchoer, D. Abdelrahman, S. N. Abdollahi, A. A. LaRocca, U. Steiner, M. Saba, I. Gunkel and B. D. Wilts, *Adv. Photon. Res.*, 2020, **1**, 2000037.
20 I. Murataj, M. Channab, E. Cara, C. F. Pirri, L. Boarino, A. Angelini and F. Ferrarese Lupi, *Adv. Opt. Mater.*, 2021, **9**, 2001933.
21 A. Alvarez-Fernandez, C. Cummins, M. Saba, U. Steiner, G. Fleury, V. Ponsinet and S. Guldin, *Adv. Opt. Mater.*, 2021, **9**, 2100175.
22 A. Noro, Y. Tomita, Y. Matsushita and E. L. Thomas, *Macromolecules*, 2016, **49**, 8971–8979.
23 A. L. Liberman-Martin, C. K. Chu and R. H. Grubbs, *Macromol. Rapid Commun.*, 2017, **38**, 1700058.
24 P. A. Mistark, S. Park, S. E. Yalcin, D. H. Lee, O. Yavuzcetin, M. T. Tuominen, T. P. Russell and M. Achermann, *ACS Nano*, 2009, **3**, 3987–3992.
25 A. Rahman, M. Liu and C. T. Black, *J. Vac. Sci. Technol. B*, 2014, **32**, 06FE02.
26 V. Abetz, *Macromol. Rapid Commun.*, 2015, **36**, 10–22.
27 S. P. Nunes, *Macromolecules*, 2016, **49**, 2905–2916.
28 P. W. Majewski and K. G. Yager, *J. Phys.: Condens. Matter*, 2016, **28**, 403002.
29 J. C. Brendel and F. H. Schacher, *Chem. – Asian J.*, 2018, **13**, 230–239.
30 M. Karayianni and S. Pispas, *J. Polym. Sci.*, 2021, **59**, 1874–1898.
31 P. Alexandridis and R. J. Spontak, *Curr. Opin. Colloid Interface Sci.*, 1999, **4**, 130–139.

32 M. R. Bockstaller, R. A. Mickiewicz and E. L. Thomas, *Adv. Mater.*, 2005, **17**, 1331–1349.
33 L. Bombalski, J. Listak and M. R. Bockstaller, *Annual Review of Nano Research*, World Scientific, 2006, vol. 1, pp. 295–336.
34 B. Sarkar and P. Alexandridis, *Prog. Polym. Sci.*, 2015, **40**, 33–62.
35 T. A. Walker, D. J. Frankowski and R. J. Spontak, *Adv. Mater.*, 2008, **20**, 879–898.
36 S. Lin and P. Theato, *Macromol. Rapid Commun.*, 2013, **34**, 1118–1133.
37 A. Darabi, P. G. Jessop and M. F. Cunningham, *Chem. Soc. Rev.*, 2016, **45**, 4391–4436.
38 H. Liu, S. Lin, Y. Feng and P. Theato, *Polym. Chem.*, 2016, **8**, 12–23.
39 Y. Li, Y.-Y. Zhang, L.-F. Hu, X.-H. Zhang, B.-Y. Du and J.-T. Xu, *Prog. Polym. Sci.*, 2018, **82**, 120–157.
40 A. A. Leniart, P. Pula, E. H.-R. Tsai and P. W. Majewski, *Macromolecules*, 2020, **53**, 11178–11189.
41 M. M. Rahman, *Macromol. Rapid Commun.*, 2021, **42**, 2100235.
42 R. Lundy, S. P. Flynn, C. Cummins, S. M. Kelleher, M. N. Collins, E. Dalton, S. Daniels, M. A. Morris and R. Enright, *Phys. Chem. Chem. Phys.*, 2017, **19**, 2805–2815.
43 A. Modi, S. M. Bhaway, B. D. Vogt, J. F. Douglas, A. Al-Enizi, A. Elzatahry, A. Sharma and A. Karim, *ACS Appl. Mater. Interfaces*, 2015, **7**, 21639–21645.
44 C. Zhang, K. A. Cavicchi, R. Li, K. G. Yager, M. Fukuto and B. D. Vogt, *Macromolecules*, 2018, **51**, 4213–4219.
45 J. Choi, J. Huh, K. R. Carter and T. P. Russell, *ACS Nano*, 2016, **10**, 7915–7925.
46 In *Polymer handbook*, ed. J. Brandrup, Wiley, Hoboken, NJ, 4th edn, 1999.
47 M. Rubinstein and R. H. Colby, *Polymer Physics*, Oxford University Press, Oxford, New York, 1st edn, 2003.
48 R. F. Blanks and J. M. Prausnitz, *Ind. Eng. Chem. Fund.*, 1964, **3**, 1–8.
49 P. J. Flory, *Principles of polymer chemistry*, Cornell University Press, Ithaca (N.Y.) London, 1992.
50 J. H. Petropoulos, *Polymeric gas separation membranes*, CRC Press Inc., New York, 1st edn, 1994, p. 635.
51 J. Jaczewska, I. Raptis, A. Budkowski, D. Goustouridis, J. Raczkowska, M. Sanopoulou, E. Pamuła, A. Bernasik and J. Rysz, *Synth. Met.*, 2007, **157**, 726–732.
52 H. Elbs and G. Krausch, *Polymer*, 2004, **45**, 7935–7942.
53 J. A. Emerson, D. T.-W. Toolan, J. R. Howse, E. M. Furst and T. H. Epps, *Macromolecules*, 2013, **46**, 6533–6540.
54 P. Alessi, A. Cortesi, P. Sacomani and E. Valles, *Macromolecules*, 1993, **26**, 6175–6179.
55 D. W. Tomlin and C. M. Roland, *Macromolecules*, 1992, **25**, 2994–2996.
56 R. C. Reid, J. M. Prausnitz and T. K. Sherwood, *The properties of gases and liquids*, McGraw-Hill, New York, 3rd edn, 1977.
57 Chemical Rubber Company, *CRC handbook of chemistry and physics: a ready-reference book of chemical and physical data*, CRC Press, Boca Raton, 84th edn, 2003/2004, 2003.
58 M. L. Huggins, *J. Phys. Chem.*, 1951, **55**, 619–620.
59 C. M. Hansen, *Hansen solubility parameters: A user's handbook*, CRC Press, Boca Raton, 2nd edn, 2007.
60 E. Stefanis and C. Panayiotou, *Int. J. Thermophys.*, 2008, **29**, 568–585.
61 T. P. Lodge and P. C. Hiemenz, *Polymer Chemistry*, CRC Press, Boca Raton, 3rd edn, 2020.
62 T. Lindvig, M. L. Michelsen and G. M. Kontogeorgis, *Fluid Phase Equilib.*, 2002, **203**, 247–260.
63 L. Leibler, *Macromolecules*, 1980, **13**, 1602–1617.
64 M. D. Whitmore and J. Noolandi, *J. Chem. Phys.*, 1990, **93**, 2946–2955.
65 T. Xu, A. V. Zvelindovsky, G. J.-A. Sevink, K. S. Lyakhova, H. Jinnai and T. P. Russell, *Macromolecules*, 2005, **38**, 10788–10798.
66 C. Liedel, C. W. Pester, M. Ruppel, V. S. Urban and A. Böker, *Macromol. Chem. Phys.*, 2012, **213**, 259–269.
67 M. Gopinadhan, P. W. Majewski, E. S. Beach and C. O. Osuji, *ACS Macro Lett.*, 2012, **1**, 184–189.
68 Y. Rokhlenko, M. Gopinadhan, C. O. Osuji, K. Zhang, C. S. O'Hern, S. R. Larson, P. Gopalan, P. W. Majewski and K. G. Yager, *Phys. Rev. Lett.*, 2015, **115**, 258302.
69 B. C. Berry, A. W. Bosse, J. F. Douglas, R. L. Jones and A. Karim, *Nano Lett.*, 2007, **7**, 2789–2794.
70 G. Singh, K. G. Yager, D.-M. Smilgies, M. M. Kulkarni, D. G. Bucknall and A. Karim, *Macromolecules*, 2012, **45**, 7107–7117.
71 D. E. Angelescu, J. H. Waller, D. H. Adamson, P. Deshpande, S. Y. Chou, R. A. Register and P. M. Chaikin, *Adv. Mater.*, 2004, **16**, 1736–1740.
72 R. L. Davis, P. M. Chaikin and R. A. Register, *Macromolecules*, 2014, **47**, 5277–5285.
73 M. Longanecker, A. Modi, A. Dobrynin, S. Kim, G. Yuan, R. Jones, S. Satija, J. Bang and A. Karim, *Macromolecules*, 2016, **49**, 8563–8571.
74 C. M. Papadakis, K. Almdal, K. Mortensen and D. Posselt, *EPL*, 1996, **36**, 289.
75 E. Helfand and Y. Tagami, *J. Chem. Phys.*, 1972, **56**, 3592–3601.
76 K. J. Hanley and T. P. Lodge, *J. Polym. Sci. B: Polym. Phys.*, 1998, **36**, 3101–3113.
77 T. P. Lodge, C. Pan, X. Jin, Z. Liu, J. Zhao, W. W. Maurer and F. S. Bates, *J. Polym. Sci., Part B: Polym. Phys.*, 1995, **33**, 2289–2293.
78 T. P. Lodge, K. J. Hanley, B. Pudil and V. Alahapperuma, *Macromolecules*, 2003, **36**, 816–822.
79 L. Zeman and D. Patterson, *Macromolecules*, 1972, **5**, 513–516.
80 B. Nandan, M. K. Vyas, M. Böhme and M. Stamm, *Macromolecules*, 2010, **43**, 2463–2473.
81 J. K. Bosworth, M. Y. Paik, R. Ruiz, E. L. Schwartz, J. Q. Huang, A. W. Ko, D.-M. Smilgies, C. T. Black and C. K. Ober, *ACS Nano*, 2008, **2**, 1396–1402.
82 D. M. Yu, D. M. Smith, H. Kim, J. K.-D. Mapas, J. Rzayev and T. P. Russell, *Macromolecules*, 2019, **52**, 3592–3600.
83 T. Hashimoto, M. Shibayama and H. Hawai, *Macromolecules*, 1983, **16**, 1093–1101.

84 J. Zhang, D. Posselt, D.-M. Smilgies, J. Perlich, K. Kyriakos, S. Jaksch and C. M. Papadakis, *Macromolecules*, 2014, **47**, 5711–5718.
85 M. W. Matsen and F. S. Bates, *Macromolecules*, 1996, **29**, 1091–1098.
86 E. B. Gowd, T. Koga, M. K. Endoh, K. Kumar and M. Stamm, *Soft Matter*, 2014, **10**, 7753–7761.
87 X. Gu, I. Gunkel, A. Hexemer and T. P. Russell, *Macromolecules*, 2016, **49**, 3373–3381.
88 K. Kim, S. Park, Y. Kim, J. Bang, C. Park and D. Y. Ryu, *Macromolecules*, 2016, **49**, 1722–1730.
89 S. Xiong, D. Li, S.-M. Hur, G. S.-W. Craig, C. G. Arges, X.-P. Qu and P. F. Nealey, *Macromolecules*, 2018, **51**, 7145–7151.
90 F. A. Jung, A. V. Berezkin, T. B. Tejsner, D. Posselt, D.-M. Smilgies and C. M. Papadakis, *Macromol. Rapid Commun.*, 2020, **41**, 2000150.
91 T. P. Lodge, B. Pudil and K. J. Hanley, *Macromolecules*, 2002, **35**, 4707–4717.
92 A. Matsushita and S. Okamoto, *Macromolecules*, 2014, **47**, 7169–7177.
93 I. Gunkel, X. Gu, Z. Sun, E. Schaible, A. Hexemer and T. P. Russell, *J. Polym. Sci., Part B: Polym. Phys.*, 2016, **54**, 331–338.
94 T. G. Fox, *Bull. Am. Phys. Soc.*, 1956, **1**, 123.
95 H. Yokoyama and E. J. Kramer, *Macromolecules*, 1998, **31**, 7871–7876.
96 H. Yokoyama, *Mater. Sci. Eng. R: Rep.*, 2006, **53**, 199–248.
97 R. Ruiz, J. K. Bosworth and C. T. Black, *Physical Review B*, 2008, **77**, 54204.
98 D. E. Bornside, C. W. Macosko and L. E. Scriven, *J. Appl. Phys.*, 1989, **66**, 5185–5193.
99 Y. Mouhamad, P. Mokarian-Tabari, N. Clarke, R. A.-L. Jones and M. Geoghegan, *J. Appl. Phys.*, 2014, **116**, 123513.
100 L. E. Scriven, *MRS Proc.*, 1988, **121**, 717.
101 T. G. Fitzgerald, R. A. Farrell, N. Petkov, C. T. Bolger, M. T. Shaw, J. P.-F. Charpin, J. P. Gleeson, J. D. Holmes and M. A. Morris, *Langmuir*, 2009, **25**, 13551–13560.
102 C. M. Stafford, K. E. Roskov, T. H. Epps and M. J. Fasolka, *Rev. Sci. Instrum.*, 2006, **77**, 023908.
103 R. L. Davis, S. Jayaraman, P. M. Chaikin and R. A. Register, *Langmuir*, 2014, **30**, 5637–5644.
104 L. Landau and B. Levich, *Acta Physicochim. URSS*, 1942, **17**, 42–54.
105 A. Modi, S. M. Bhaway, B. D. Vogt, J. F. Douglas, A. Al-Enizi, A. Elzatahry, A. Sharma and A. Karim, *ACS Appl. Mater. Interfaces*, 2015, **7**, 21639–21645.
106 T. Bucher, V. Filiz, C. Abetz and V. Abetz, *Membranes*, 2018, **8**, 57.
107 M. Faustini, B. Louis, P. A. Albouy, M. Kuemmel and D. Grosso, *J. Phys. Chem. C*, 2010, **114**, 7637–7645.
108 A. Sidorenko, I. Tokarev, S. Minko and M. Stamm, *J. Am. Chem. Soc.*, 2003, **125**, 12211–12216.
109 A. Melninkaitis, K. Juškevičius, M. Maciulevičius, V. Sirutkaitis, A. Beganskienė, I. Kazadojev, A. Kareiva and D. Perednis, *Laser-Induced Damage in Optical Materials: 2006*, SPIE, 2007, vol. 6403, pp. 437–444.
110 D.-F. Lii, J.-L. Huang, L.-J. Tsui and S.-M. Lee, *Surf. Coat. Technol.*, 2002, **150**, 269–276.
111 H. Benkreira, *Chem. Eng. Sci.*, 2004, **59**, 2745–2751.
112 H. Hu, S. Rangou, M. Kim, P. Gopalan, V. Filiz, A. Avgeropoulos and C. O. Osuji, *ACS Nano*, 2013, **7**, 2960–2970.
113 K. Toth, C. O. Osuji, K. G. Yager and G. S. Doerk, *Rev. Sci. Instrum.*, 2020, **91**, 013701.
114 M. S. Onses, C. Song, L. Williamson, E. Sutanto, P. M. Ferreira, A. G. Alleyne, P. F. Nealey, H. Ahn and J. A. Rogers, *Nat. Nanotechnol.*, 2013, **8**, 667–675.
115 M. S. Onses, A. Ramírez-Hernández, S.-M. Hur, E. Sutanto, L. Williamson, A. G. Alleyne, P. F. Nealey, J. J. de Pablo and J. A. Rogers, *ACS Nano*, 2014, **8**, 6606–6613.
116 M. L. Wadley, I.-F. Hsieh, K. A. Cavicchi and S. Z.-D. Cheng, *Macromolecules*, 2012, **45**, 5538–5545.
117 K. W. Gotrik and C. A. Ross, *Nano Lett.*, 2013, **13**, 5117–5122.
118 D. R. Barbero and U. Steiner, *Phys. Rev. Lett.*, 2009, **102**, 248303.
119 X. Zhang, J. F. Douglas and R. L. Jones, *Soft Matter*, 2012, **8**, 4980–4987.
120 T. Inoue, T. Soen, T. Hashimoto and H. Kawai, *J. Polym. Sci., Part A-2*, 1969, **7**, 1283–1301.
121 F. S. Bates, C. V. Berney and R. E. Cohen, *Macromolecules*, 1983, **16**, 1101–1108.
122 G. Kim and M. Libera, *Macromolecules*, 1998, **31**, 2670–2672.
123 R. Guo, H. Huang, B. Du and T. He, *J. Phys. Chem. B*, 2009, **113**, 2712–2724.
124 J. N.-L. Albert, W.-S. Young, R. L. Lewis, T. D. Bogart, J. R. Smith and T. H. Epps, *ACS Nano*, 2012, **6**, 459–466.
125 S. H. Kim, M. J. Misner, T. Xu, M. Kimura and T. P. Russell, *Adv. Mater.*, 2004, **16**, 226–231.
126 Y. Chen, H. Huang, Z. Hu and T. He, *Langmuir*, 2004, **20**, 3805–3808.
127 J. Hayat, I. Mitra, Y. Qiao, G. E. Stein and C. Tang, *Eur. Polym. J.*, 2015, **71**, 476–489.
128 D. W. Breiby, O. Bunk, W. Pisula, T. I. Sølling, A. Tracz, T. Pakula, K. Müllen and M. M. Nielsen, *J. Am. Chem. Soc.*, 2005, **127**, 11288–11293.
129 C. Tang, W. Wu, D.-M. Smilgies, K. Matyjaszewski and T. Kowalewski, *J. Am. Chem. Soc.*, 2011, **133**, 11802–11809.
130 M. Kimura, M. J. Misner, T. Xu, S. H. Kim and T. P. Russell, *Langmuir*, 2003, **19**, 9910–9913.
131 W. A. Phillip, R. M. Dorin, J. Werner, E. M.-V. Hoek, U. Wiesner and M. Elimelech, *Nano Lett.*, 2011, **11**, 2892–2900.
132 S. Sourirajan, *Ind. Eng. Chem. Fund.*, 1963, **2**, 51–55.
133 S. Rangou, K. Buhr, V. Filiz, J. I. Clodt, B. Lademann, J. Hahn, A. Jung and V. Abetz, *J. Membr. Sci.*, 2014, **451**, 266–275.
134 R. A. Mulvenna, J. L. Weidman, B. Jing, J. A. Pople, Y. Zhu, B. W. Boudouris and W. A. Phillip, *J. Membr. Sci.*, 2014, **470**, 246–256.
135 K.-V. Peinemann, V. Abetz and P. F.-W. Simon, *Nat. Mater.*, 2007, **6**, 992–996.
136 W. A. Phillip, B. O'Neill, M. Rodwogin, M. A. Hillmyer and E. L. Cussler, *ACS Appl. Mater. Interfaces*, 2010, **2**, 847–853.

137 D. S. Marques, U. Vainio, N. M. Chaparro, V. M. Calo, A. R. Bezahd, J. W. Pitera, K. V. Peinemann and S. P. Nunes, *Soft Matter*, 2013, **9**, 5557–5564.
138 X. Qiu, H. Yu, M. Karunakaran, N. Pradeep, S. P. Nunes and K.-V. Peinemann, *ACS Nano*, 2013, **7**, 768–776.
139 M. Radjabian and V. Abetz, *Adv. Mater.*, 2015, **27**, 352–355.
140 F. Schacher, M. Ulbricht and A. H.-E. Müller, *Adv. Funct. Mater.*, 2009, **19**, 1040–1045.
141 Y. Zhang, N. E. Almodovar-Arbelo, J. L. Weidman, D. S. Corti, B. W. Boudouris and W. A. Phillip, *npj Clean Water*, 2018, **1**, 1–14.
142 W. A. Phillip, M. A. Hillmyer and E. L. Cussler, *Macromolecules*, 2010, **43**, 7763–7770.
143 Y. Zhang, J. L. Sargent, B. W. Boudouris and W. A. Phillip, *J. Appl. Polym. Sci.*, 2015, **132**, 41683.
144 C. Yang, G. Zhu, Z. Yi, Y. Zhou and C. Gao, *Chem. Eng. J.*, 2021, **424**, 128912.
145 C. Park, C. De Rosa and E. L. Thomas, *Macromolecules*, 2001, **34**, 2602–2606.
146 H. Jung, S. Woo, Y. Choe, D. Y. Ryu, J. Huh and J. Bang, *ACS Macro Lett.*, 2015, **4**, 656–660.
147 D. W. Weller, L. Galuska, W. Wang, D. Ehlenburg, K. Hong and X. Gu, *Macromolecules*, 2019, **52**, 5026–5032.
148 A. A. Leniart, P. Pula, R. W. Style and P. W. Majewski, *ACS Macro Lett.*, 2022, **11**, 121–126.
149 T. Hashimoto, J. Bodycomb, Y. Funaki and K. Kimishima, *Macromolecules*, 1999, **32**, 952–954.
150 M. Gopinadhan, P. W. Majewski, Y. Choo and C. O. Osuji, *Phys. Rev. Lett.*, 2013, **110**, 078301.
151 W. Cao, S. Xia, M. Appold, N. Saxena, L. Bießmann, S. Grott, N. Li, M. Gallei, S. Bernstorff and P. Müller-Buschbaum, *Sci. Rep.*, 2019, **9**, 18269.
152 S. Park, Y. Kim, W. Lee, S.-M. Hur and D. Y. Ryu, *Macromolecules*, 2017, **50**, 5033–5041.
153 G. Nelson, C. S. Drapes, M. A. Grant, R. Gnabasik, J. Wong and A. Baruth, *Micromachines*, 2018, **9**, 271.
154 K. W. Gotrik, A. F. Hannon, J. G. Son, B. Keller, A. Alexander-Katz and C. A. Ross, *ACS Nano*, 2012, **6**, 8052–8059.
155 H. Elbs, C. Drummer, V. Abetz and G. Krausch, *Macromolecules*, 2002, **35**, 5570–5577.
156 X. Gu, I. Gunkel, A. Hexemer and T. P. Russell, *Colloid Polym. Sci.*, 2014, **292**, 1795–1802.
157 C. Cummins, P. Mokarian-Tabari, P. Andreazza, C. Sinturel and M. A. Morris, *ACS Appl. Mater. Interfaces*, 2016, **8**, 8295–8304.
158 J. Peng, D. H. Kim, W. Knoll, Y. Xuan, B. Li and Y. Han, *J. Chem. Phys.*, 2006, **125**, 064702.
159 E. Kim, H. Ahn, S. Park, H. Lee, M. Lee, S. Lee, T. Kim, E.-A. Kwak, J. H. Lee, X. Lei, J. Huh, J. Bang, B. Lee and D. Y. Ryu, *ACS Nano*, 2013, **7**, 1952–1960.
160 J. Xu, K. Wang, J. Li, H. Zhou, X. Xie and J. Zhu, *Macromolecules*, 2015, **48**, 2628–2636.
161 M. Cetintas and M. Kamperman, *Polymer*, 2016, **107**, 387–397.
162 K. Aissou, M. Mumtaz, P. Marcasuzaa, C. Brochon, E. Cloutet, G. Fleury and G. Hadziioannou, *Small*, 2017, **13**, 1603184.
163 S. Lee, L.-C. Cheng, K. G. Yager, M. Mumtaz, K. Aissou and C. A. Ross, *Macromolecules*, 2019, **52**, 1853–1863.
164 C. Sinturel, M. Vayer, M. Morris and M. A. Hillmyer, *Macromolecules*, 2013, **46**, 5399–5415.
165 C. Jin, B. C. Olsen, E. J. Luber and J. M. Buriak, *Chem. Mater.*, 2017, **29**, 176–188.
166 D. H. Lee, H. Cho, S. Yoo and S. Park, *J. Colloid Interface Sci.*, 2012, **383**, 118–123.
167 W. Bai, A. F. Hannon, K. W. Gotrik, H. K. Choi, K. Aissou, G. Liontos, K. Ntetsikas, A. Alexander-Katz, A. Avgeropoulos and C. A. Ross, *Macromolecules*, 2014, **47**, 6000–6008.
168 A. Baruth, M. Seo, C. H. Lin, K. Walster, A. Shankar, M. A. Hillmyer and C. Leighton, *ACS Appl. Mater. Interfaces*, 2014, **6**, 13770–13781.
169 W.-H. Huang, P.-Y. Chen and S.-H. Tung, *Macromolecules*, 2012, **45**, 1562–1569.
170 A. Knoll, R. Magerle and G. Krausch, *J. Chem. Phys.*, 2004, **120**, 1105–1116.
171 M. Y. Paik, J. K. Bosworth, D.-M. Smilges, E. L. Schwartz, X. Andre and C. K. Ober, *Macromolecules*, 2010, **43**, 4253–4260.
172 Y. Tada, H. Yoshida, Y. Ishida, T. Hirai, J. K. Bosworth, E. Dobisz, R. Ruiz, M. Takenaka, T. Hayakawa and H. Hasegawa, *Macromolecules*, 2012, **45**, 292–304.
173 M. A. Chavis, D.-M. Smilgies, U. B. Wiesner and C. K. Ober, *Adv. Funct. Mater.*, 2015, **25**, 3057–3065.
174 G. S. Doerk, R. Li, M. Fukuto and K. G. Yager, *Macromolecules*, 2020, **53**, 1098–1113.
175 A. V. Berezkin, F. Jung, D. Posselt, D.-M. Smilgies and C. M. Papadakis, *Adv. Funct. Mater.*, 2018, **28**, 1706226.
176 H. Hulkkonen, T. Salminen and T. Niemi, *Soft Matter*, 2019, **15**, 7909–7917.
177 A. Selkirk, N. Prochukhan, R. Lundy, C. Cummins, R. Gatensby, R. Kilbride, A. Parnell, J. Baez Vasquez, M. Morris and P. Mokarian-Tabari, *Macromolecules*, 2021, **54**, 1203–1215.
178 J. N.-L. Albert, T. D. Bogart, R. L. Lewis, K. L. Beers, M. J. Fasolka, J. B. Hutchison, B. D. Vogt and T. H. Epps, *Nano Lett.*, 2011, **11**, 1351–1357.
179 S. Hüttner, M. Sommer, A. Chiche, G. Krausch, U. Steiner and M. Thelakkat, *Soft Matter*, 2009, **5**, 4206–4211.
180 C. Sinturel, D. Grosso, M. Boudot, H. Amenitsch, M. A. Hillmyer and A. Pineau, *ACS Appl. Mater. Interfaces*, 2014, **7**, 12146–12152.
181 L. Xu, Z. Zou, H. Zhang and T. Shi, *Chem. Res. Chin. Univ.*, 2017, **33**, 833–838.
182 M. Y. Efremov and P. F. Nealey, *Polymer*, 2022, **238**, 124417.
183 A. Laschitsch, C. Bouchard, J. Habicht, M. Schimmel, J. Rühe and D. Johannsmann, *Macromolecules*, 1999, **32**, 1244–1251.
184 K. Takano, T. Nyu, T. Maekawa, T. Seki, R. Nakatani, T. Komamura, T. Hayakawa and T. Hayashi, *RSC Adv.*, 2019, **10**, 70–75.
185 C. Harrison, D. H. Adamson, Z. Cheng, J. M. Sebastian, S. Sethuraman, D. A. Huse, R. A. Register and P. M. Chaikin, *Science*, 2000, **290**, 1558–1560.

186 J. Hahm and S. J. Sibener, *J. Chem. Phys.*, 2001, **114**, 4730–4740.
187 J. G. Raybin and S. J. Sibener, *Macromolecules*, 2019, **52**, 5985–5994.
188 D. Posselt, J. Zhang, D.-M. Smilgies, A. V. Berezkin, I. I. Potemkin and C. M. Papadakis, *Prog. Polym. Sci.*, 2017, **66**, 80–115.
189 Z. Di, D. Posselt, D.-M. Smilgies and C. M. Papadakis, *Macromolecules*, 2010, **43**, 418–427.
190 I. Gunkel, X. Gu, Z. Sun, E. Schaible, A. Hexemer and T. P. Russell, *J. Polym. Sci. Part B: Polym. Phys.*, 2016, **54**, 331–338.
191 C. K. Shelton, R. L. Jones, J. A. Dura and T. H. Epps, *Macromolecules*, 2016, **49**, 7525–7534.
192 J. W. Jeong, Y. H. Hur, H. Kim, J. M. Kim, W. I. Park, M. J. Kim, B. J. Kim and Y. S. Jung, *ACS Nano*, 2013, **7**, 6747–6757.
193 B. C. Stahl, E. J. Kramer, C. J. Hawker and N. A. Lynd, *J. Polym. Sci., Part B: Polym. Phys.*, 2017, **55**, 1125–1130.
194 S. P. Paradiso, K. T. Delaney, C. J. García-Cervera, H. D. Ceniceros and G. H. Fredrickson, *Macromolecules*, 2016, **49**, 1743–1751.
195 H. Park, S. Jo, B. Kang, K. Hur, S. S. Oh, D. Y. Ryu and S. Lee, *Nanophotonics*, 2022, **11**, 2583–2615.
196 S. Park, Y. Kim, H. Ahn, J. H. Kim, P. J. Yoo and D. Y. Ryu, *Sci. Rep.*, 2016, **6**, 36326.
197 C. Cummins, A. Alvarez-Fernandez, A. Bentaleb, G. Hadziioannou, V. Ponsinet and G. Fleury, *Langmuir*, 2020, **36**, 13872–13880.
198 X. Gu, I. Gunkel, A. Hexemer, W. Gu and T. P. Russell, *Adv. Mater.*, 2014, **26**, 273–281.
199 R. Guo, H. Huang, Y. Chen, Y. Gong, B. Du and T. He, *Macromolecules*, 2008, **41**, 890–900.
200 L.-Y. Shi, F. Liao, L.-C. Cheng, S. Lee, R. Ran, Z. Shen and C. A. Ross, *ACS Macro Lett.*, 2019, **8**, 852–858.
201 Y.-H. Wu, T.-Y. Lo, M.-S. She and R.-M. Ho, *ACS Appl. Mater. Interfaces*, 2015, **7**, 16536–16547.
202 Y. Cong, W. Zhai and C. Wu, *Soft Mater.*, 2021, **19**, 117–128.
203 S. Kim, G. Jeon, S. W. Heo, H. J. Kim, S. B. Kim, T. Chang and J. K. Kim, *Soft Matter*, 2013, **9**, 5550–5556.
204 J. Peng, Y. Xuan, H. Wang, Y. Yang, B. Li and Y. Han, *J. Chem. Phys.*, 2004, **120**, 11163–11170.
205 Y. Li, H. Huang, T. He and Y. Gong, *Appl. Surf. Sci.*, 2011, **257**, 8093–8101.
206 Y. S. Jung and C. A. Ross, *Adv. Mater.*, 2009, **21**, 2540–2545.
207 Y. J. Choi, M. H. Byun, T. W. Park, S. Choi, J. Bang, H. Jung, J.-H. Cho, S.-H. Kwon, K. H. Kim and W. I. Park, *ACS Appl. Nano Mater.*, 2019, **2**, 1294–1301.
208 C. Luo, W. Huang and Y. Han, *Macromol. Rapid Commun.*, 2009, **30**, 515–520.
209 H. Jung, W. H. Shin, T. W. Park, Y. J. Choi, Y. J. Yoon, S. H. Park, J.-H. Lim, J.-D. Kwon, J. W. Lee, S.-H. Kwon, G. H. Seong, K. H. Kim and W. I. Park, *Nanoscale*, 2019, **11**, 8433–8441.
210 L. Cheng, J. W. Simonaitis, K. R. Gadelrab, M. Tahir, Y. Ding, A. Alexander-Katz and C. A. Ross, *Small*, 2020, **16**, 1905509.
211 A. Subramanian, G. Doerk, K. Kisslinger, D. H. Yi, R. B. Grubbs and C.-Y. Nam, *Nanoscale*, 2019, **11**, 9533–9546.
212 L.-Y. Shi, A. Subramanian, L. Weng, S. Lee, K. Kisslinger, C.-Y. Nam and C. A. Ross, *Nanoscale*, 2022, **14**, 1807–1813.
213 G. Ginige, Y. Song, B. C. Olsen, E. J. Luber, C. T. Yavuz and J. M. Buriak, *ACS Appl. Mater. Interfaces*, 2021, **13**, 28639–28649.
214 J. E. Seppala, R. L. Lewis and T. H. Epps, *ACS Nano*, 2012, **6**, 9855–9862.
215 J. M. Kim, Y. J. Kim, W. I. Park, Y. H. Hur, J. W. Jeong, D. M. Sim, K. M. Baek, J. H. Lee, M. J. Kim and Y. S. Jung, *Adv. Funct. Mater.*, 2015, **25**, 306–315.
216 P. Mokarian-Tabari, C. Cummins, S. Rasappa, C. Simao, C. M. Sotomayor Torres, J. D. Holmes and M. A. Morris, *Langmuir*, 2014, **30**, 10728–10739.
217 D. Borah, M. T. Shaw, J. D. Holmes and M. A. Morris, *ACS Appl. Mater. Interfaces*, 2013, **5**, 2004–2012.
218 X. Zhang, K. D. Harris, N. L.-Y. Wu, J. N. Murphy and J. M. Buriak, *ACS Nano*, 2010, **4**, 7021–7029.
219 X. Zhang, J. N. Murphy, N. L.-Y. Wu, K. D. Harris and J. M. Buriak, *Macromolecules*, 2011, **44**, 9752–9757.
220 R. A. Segalman, H. Yokoyama and E. J. Kramer, *Adv. Mater.*, 2001, **13**, 1152–1155.
221 I. Bita, J. K.-W. Yang, S. J. Yeon, C. A. Ross, E. L. Thomas and K. K. Berggren, *Science*, 2008, **321**, 939–943.
222 R. Ruiz, H. Kang, F. A. Detcheverry, E. Dobisz, D. S. Kercher, T. R. Albrecht, J. J. De Pablo and P. F. Nealey, *Science*, 2008, **321**, 936–939.
223 C.-C. Liu, A. Ramírez-Hernández, E. Han, G. S.-W. Craig, Y. Tada, H. Yoshida, H. Kang, S. Ji, P. Gopalan, J. J. de Pablo and P. F. Nealey, *Macromolecules*, 2013, **46**, 1415–1424.
224 M. J. Maher, C. T. Rettner, C. M. Bates, G. Blachut, M. C. Carlson, W. J. Durand, C. J. Ellison, D. P. Sanders, J. Y. Cheng and C. G. Willson, *ACS Appl. Mater. Interfaces*, 2015, **7**, 3323–3328.
225 S. Ji, L. Wan, C.-C. Liu and P. F. Nealey, *Prog. Polym. Sci.*, 2016, **54–55**, 76–127.
226 Y. S. Jung and C. A. Ross, *Nano Lett.*, 2007, **7**, 2046–2050.
227 K. Lee, M. Kreider, W. Bai, L.-C. Cheng, S. S. Dinachali, K.-H. Tu, T. Huang, K. Ntetsikas, G. Liontos, A. Avgeropoulos and C. A. Ross, *Nanotechnology*, 2016, **27**, 465301.
228 L.-C. Cheng, W. Bai, E. F. Martin, K.-H. Tu, K. Ntetsikas, G. Liontos, A. Avgeropoulos and C. A. Ross, *Nanotechnology*, 2017, **28**, 145301.
229 C. Tang, J. Bang, G. E. Stein, G. H. Fredrickson, C. J. Hawker, E. J. Kramer, M. Sprung and J. Wang, *Macromolecules*, 2008, **41**, 4328–4339.
230 H. K. Choi, J.-B. Chang, A. F. Hannon, J. K.-W. Yang, K. K. Berggren, A. Alexander-Katz and C. A. Ross, *Nano Futures*, 2017, **1**, 015001.
231 S. Lee, L.-C. Cheng, K. R. Gadelrab, K. Ntetsikas, D. Moschovas, K. G. Yager, A. Avgeropoulos, A. Alexander-Katz and C. A. Ross, *ACS Nano*, 2018, **12**, 6193–6202.
232 L.-C. Cheng, K. R. Gadelrab, K. Kawamoto, K. G. Yager, J. A. Johnson, A. Alexander-Katz and C. A. Ross, *Nano Lett.*, 2018, **18**, 4360–4369.

233 L.-Y. Shi, J. Lan, S. Lee, L.-C. Cheng, K. G. Yager and C. A. Ross, *ACS Nano*, 2020, **14**, 4289–4297.
234 L.-Y. Shi, C. Yin, B. Zhou, W. Xia, L. Weng and C. A. Ross, *Macromolecules*, 2021, **54**, 1657–1664.
235 S. Xiong, L. Wan, Y. Ishida, Y.-A. Chapuis, G. S.-W. Craig, R. Ruiz and P. F. Nealey, *ACS Nano*, 2016, **10**, 7855–7865.
236 L. Wan, S. Ji, C.-C. Liu, G. S.-W. Craig and P. F. Nealey, *Soft Matter*, 2016, **12**, 2914–2922.
237 R. Liu, H. Huang, Z. Sun, A. Alexander-Katz and C. A. Ross, *ACS Nano*, 2021, **15**, 16266–16276.
238 T.-C. Wang, H.-Y. Hsueh and R.-M. Ho, *Chem. Mater.*, 2010, **22**, 4642–4651.
239 C.-J. Chu, M.-H. Cheng, P.-Y. Chung, M.-H. Chi, K.-S. Jeng and J.-T. Chen, *Int. J. Polym. Mater. Polym. Biomater.*, 2016, **65**, 695–701.
240 Y.-H. Tseng, Y.-L. Lin, J.-H. Ho, C.-T. Chang, Y.-C. Fan, M.-H. Shen and J.-T. Chen, *Polymer*, 2021, **228**, 123859.
241 S. Ok, M. Vayer and C. Sinturel, *Soft Matter*, 2021, **17**, 7430–7458.
242 A. A. Abate, G. T. Vu, A. D. Pezzutti, N. A. García, R. L. Davis, F. Schmid, R. A. Register and D. A. Vega, *Macromolecules*, 2016, **49**, 7588–7596.
243 G. Singh, S. Batra, R. Zhang, H. Yuan, K. G. Yager, M. Cakmak, B. Berry and A. Karim, *ACS Nano*, 2013, **7**, 5291–5299.
244 P. W. Majewski and K. G. Yager, *Macromolecules*, 2015, **48**, 4591–4598.
245 M. N. Basutkar, P. W. Majewski, G. S. Doerk, K. Toth, C. O. Osuji, A. Karim and K. G. Yager, *Macromolecules*, 2019, **52**, 7224–7233.
246 Z. Qiang, L. Zhang, G. E. Stein, K. A. Cavicchi and B. D. Vogt, *Macromolecules*, 2014, **47**, 1109–1116.
247 Z. Qiang, Y. Zhang, J. A. Groff, K. A. Cavicchi and B. D. Vogt, *Soft Matter*, 2014, **10**, 6068–6076.
248 M. Luo, D. M. Scott and T. H. Epps, *ACS Macro Lett.*, 2015, **4**, 516–520.
249 Z. Qiang, Y. Zhang, Y. Wang, S. M. Bhaway, K. A. Cavicchi and B. D. Vogt, *Carbon*, 2015, **82**, 51–59.
250 Z. Qiang, M. L. Wadley, B. D. Vogt and K. A. Cavicchi, *J. Polym. Sci., Part B: Polym. Phys.*, 2015, **53**, 1058–1064.
251 C. K. Shelton, R. L. Jones and T. H. Epps, *Macromolecules*, 2017, **50**, 5367–5376.
252 S. H. Sung, W. B. Farnham, H. E. Burch, Y. Brun, K. Qi and T. H. Epps III, *J. Polym. Sci., Part B: Polym. Phys.*, 2019, **57**, 1663–1672.
253 H. Kang, K. Kim and B.-H. Sohn, *Nanotechnology*, 2020, **31**, 455302.
254 Y. C. Kim, T. J. Shin, S.-M. Hur, S. J. Kwon and S. Y. Kim, *Sci. Adv.*, 2019, **5**, eaaw3974.
255 E. R. Gottlieb, P. Dimitrakellis, D. G. Vlachos and T. H. Epps, *ACS Appl. Polym. Mater.*, 2022, **4**, 682–691.
256 J. P. Singer, K. W. Gotrik, J. H. Lee, S. E. Kooi, C. A. Ross and E. L. Thomas, *Polymer*, 2014, **55**, 1875–1882.
257 F. F. Lupi, T. J. Giammaria, M. Ceresoli, G. Seguini, K. Sparnacci, D. Antonioli, V. Gianotti, M. Laus and M. Perego, *Nanotechnology*, 2013, **24**, 315601.
258 G. Seguini, F. Zanenga, T. J. Giammaria, M. Ceresoli, K. Sparnacci, D. Antonioli, V. Gianotti, M. Laus and M. Perego, *ACS Appl. Mater. Interfaces*, 2016, **8**, 8280–8288.
259 T. J. Giammaria, F. Ferrarese Lupi, G. Seguini, K. Sparnacci, D. Antonioli, V. Gianotti, M. Laus and M. Perego, *ACS Appl. Mater. Interfaces*, 2017, **9**, 31215–31223.
260 X. Zhang, K. G. Yager, S. Kang, N. J. Fredin, B. Akgun, S. Satija, J. F. Douglas, A. Karim and R. L. Jones, *Macromolecules*, 2010, **43**, 1117–1123.
261 M. Perego, F. Ferrarese Lupi, M. Ceresoli, T. J. Giammaria, G. Seguini, E. Enrico, L. Boarino, D. Antonioli, V. Gianotti, K. Sparnacci and M. Laus, *J. Mater. Chem. C*, 2014, **2**, 6655–6664.
262 K. Sparnacci, R. Chiarcos, V. Gianotti, M. Laus, T. J. Giammaria, M. Perego, G. Munaò, G. Milano, A. De Nicola, M. Haese, L. P. Kreuzer, T. Widmann and P. Müller-Buschbaum, *ACS Appl. Mater. Interfaces*, 2020, **12**, 7777–7787.
263 M. Fang, L. Tao, W. Wu, Q. Wei, Y. Xia, P. Li, X. Ran, Q. Zhong, G. Xing, L. Song, P. Müller-Buschbaum, H. Zhang and Y. Chen, *J. Energy Chem.*, 2021, **61**, 8–14.
264 IEEE International Roadmap for Devices and Systems – IEEE IRDSTM, **https://irds.ieee.org/** (accessed March 22, 2022).
265 H. J. Dai, N. P. Balsara, B. A. Garetz and M. C. Newstein, *Phys. Rev. Lett.*, 1996, **77**, 3677–3680.
266 S. Ji, C.-C. Liu, W. Liao, A. L. Fenske, G. S.-W. Craig and P. F. Nealey, *Macromolecules*, 2011, **44**, 4291–4300.
267 I. P. Campbell, C. He and M. P. Stoykovich, *ACS Macro Lett.*, 2013, **2**, 918–923.
268 J. Li, P. A. Rincon-Delgadillo, H. S. Suh, G. Mannaert and P. F. Nealey, *JM3.1*, 2019, **18**, 043502.
269 C. Harrison, Z. Cheng, S. Sethuraman, D. A. Huse, P. M. Chaikin, D. A. Vega, J. M. Sebastian, R. A. Register and D. H. Adamson, *Phys. Rev. E*, 2002, **66**, 011706.
270 J. N. Murphy, K. D. Harris and J. M. Buriak, *PLoS One*, 2015, **10**, e0133088.
271 X. Gu, J. Reinspach, B. J. Worfolk, Y. Diao, Y. Zhou, H. Yan, K. Gu, S. Mannsfeld, M. F. Toney and Z. Bao, *ACS Appl. Mater. Interfaces*, 2016, **8**, 1687–1694.
272 Z. Sun and T. P. Russell, *J. Polym. Sci., Part B: Polym. Phys.*, 2017, **55**, 980–989.
273 J. A. Dolan, K. Korzeb, R. Dehmel, K. C. Gödel, M. Stefik, U. Wiesner, T. D. Wilkinson, J. J. Baumberg, B. D. Wilts, U. Steiner and I. Gunkel, *Small*, 2018, **14**, 1802401.
274 D.-M. Smilgies, *J Appl Cryst*, 2009, **42**, 1030–1034.
275 A. M. Welander, H. Kang, K. O. Stuen, H. H. Solak, M. Müller, J. J. de Pablo and P. F. Nealey, *Macromolecules*, 2008, **41**, 2759–2761.
276 C. Harrison, Z. Cheng, S. Sethuraman, D. A. Huse, P. M. Chaikin, D. A. Vega, J. M. Sebastian, R. A. Register and D. H. Adamson, *Phys. Rev. E*, 2002, **66**, 011706.
277 C. Harrison, D. E. Angelescu, M. Trawick, Z. Cheng, D. A. Huse, P. M. Chaikin, D. A. Vega, J. M. Sebastian, R. A. Register and D. H. Adamson, *EPL*, 2004, **67**, 800.
278 C. T. Black and K. W. Guarini, *J. Polym. Sci., Part A: Polym. Chem.*, 2004, **42**, 1970–1975.

279 D. A. Vega, C. K. Harrison, D. E. Angelescu, M. L. Trawick, D. A. Huse, P. M. Chaikin and R. A. Register, *Phys. Rev. E*, 2005, **71**, 061803.
280 R. Ruiz, R. L. Sandstrom and C. T. Black, *Adv. Mater.*, 2007, **19**, 587–591.
281 H. J. Ryu, D. B. Fortner, S. Lee, R. Ferebee, M. De Graef, K. Misichronis, A. Avgeropoulos and M. R. Bockstaller, *Macromolecules*, 2013, **46**, 204–215.
282 M. Ceresoli, F. G. Volpe, G. Seguini, D. Antonioli, V. Gianotti, K. Sparnacci, M. Laus and M. Perego, *J. Mater. Chem. C*, 2015, **3**, 8618–8624.
283 P. W. Majewski and K. G. Yager, *ACS Nano*, 2015, **9**, 3896–3906.
284 M. Fernández-Regúlez, E. Solano, L. Evangelio, S. Gottlieb, C. Pinto-Gómez, G. Rius, J. Fraxedas, E. Gutiérrez-Fernández, A. Nogales, M. C. García-Gutiérrez, T. A. Ezquerra and F. Pérez-Murano, *J. Synchrotron Rad.*, 2020, **27**, 1278–1288.
285 G. Seguini, F. Zanenga, M. Laus and M. Perego, *Phys. Rev. Mater.*, 2018, **2**, 055605.
286 N. L.-Y. Wu, X. Zhang, J. N. Murphy, J. Chai, K. D. Harris and J. M. Buriak, *Nano Lett.*, 2012, **12**, 264–268.
287 S. Pinge, Y. Qiu, V. Monreal, D. Baskaran, A. Ravirajan and Y. L. Joo, *Phys. Chem. Chem. Phys.*, 2020, **22**, 478–488.
288 W. Li and M. Müller, *Annu. Rev. Chem. Biomol. Eng.*, 2015, **6**, 187–216.
289 S.-M. Hur, V. Thapar, A. Ramírez-Hernández, P. F. Nealey and J. J. de Pablo, *ACS Nano*, 2018, **12**, 9974–9981.
290 Y. Ren and M. Müller, *Macromolecules*, 2020, **53**, 5337–5349.
291 W. Shi, *J. Phys. Chem. Lett.*, 2020, **11**, 2724–2730.
292 T. Hu, Y. Ren, L. Zhang and W. Li, *Macromolecules*, 2021, **54**, 773–782.
293 T. Hu, Y. Ren and W. Li, *Macromolecules*, 2021, **54**, 8024–8032.
294 A. F. Hannon, W. Bai, A. Alexander-Katz and C. A. Ross, *Soft Matter*, 2015, **11**, 3794–3805.
295 A. J. Peters, R. A. Lawson, B. D. Nation, P. J. Ludovice and C. L. Henderson, *JM3.1*, 2016, **15**, 013508.
296 X. Xu, X. Man, M. Doi, Z. Ou-Yang and D. Andelman, *Macromolecules*, 2019, **52**, 9321–9333.

